# A review of computational reconstruction of interaction in superresolution microscopy: from colocalization to closing the multichannel gap

Ben Cardoen[a,c], Hanene Ben Yedder[a], Ivan Robert Nabi[b,c], Ghassan Hamarneh[a]

[a]*Simon Fraser University, Department of Computing Science 8888 University Drive Burnaby, V5A 1S6, British Columbia, Canada*
[b]*University of British Columbia, School of Biomedical Engineering 2222 Health Sciences Mall, Vancouver, V6T 1Z3, British Columbia, Canada*
[c]*University of British Columbia, Life Sciences Institute 2350 Health Sciences Mall, Vancouver, V6T 1Z3, British Columbia, Canada*

**Abstract**

Cellular function is defined by pathways that, in turn, are determined by distance-mediated interactions between and within subcellular organelles, protein complexes, and macromolecular structures. Multichannel Super Resolution Microscopy (SRM) is uniquely placed to quantify distance-mediated interactions at the nanometer scale with its ability to label individual biological targets with independent markers that fluoresce in different spectra. We review novel computational methods that quantify interaction from multichannel SRM data in both point-cloud and voxel form to meet the increasing adoption of multichannel SRM in life sciences. SRM specific factors that can compromise interaction analysis are discussed in detail. Different classes of interactions are decomposed based on distinct representative cell biology use cases, the underappreciated non-linear physics of their scale, and the development of specialized methods for those use case. An abstract mathematical model is introduced to facilitate the comparison and evaluation of interaction reconstruction methods and to quantify the computational bottlenecks. We discuss the different strategies for validation of interaction analysis results with sparse or incomplete ground truth data. Finally, evolving trends and future directions are presented, highlighting the 'multichannel gap', where interaction analysis is trailing behind the rapid increase in novel multichannel SRM acquisitions.

## Contents

## 1. Introduction

Cellular health is governed by spatio-temporal interactions among subcellular organelles, protein complexes, and macromolecular structures. In this paper, we review modern computational methods, i.e. those that adopt mathematical, algorithmic, or computerized approaches to interaction analysis, in multichannel SRM. We define interaction analysis as the set of tasks that span detecting, characterizing, quantifying, and gaining insight from the relations between the communicating fluorescently labeled objects across different scales.

### *1.1. Superresolution microscopy (SRM) captures mesoscale (0-250 nm) interactions critical to cellular function*

SRM is an umbrella term for novel imaging modalities that bypass the diffraction limit (~250 nm lateral) using optical, physical, chemical, and computational methods. Interaction between objects requires precise localization. In microscopy, the 'precision' of a system describes the minimum observable distance $\delta_o$ between any two objects. The 'precision' of a multichannel acquisition is a complex function of the per-object localization uncertainty $\epsilon$ (Section 3.2, Eq. (15)). SRM modalities can localize objects in cells with a precision of up to two to five nm [6]. Although electron microscopy (EM) can quantify cellular structures and proteins with higher precision (<1 nm), it is costly, invasive to the specimen, and primarily applicable to fixed cells. In contrast, in multichannel SRM acquisitions, each channel represents a different fluorescent label or probe that selectively binds to specific targets of interest, such as organelles or specific proteins. Fig. 1 shows visual examples of some SRM modalities in point cloud and voxel form. SRM modalities use several mechanisms to bypass the diffraction limit. For example, emissions can be isolated if they only emit fluorescence stochastically with a low probability (e.g. in direct stochastic optical reconstruction microscopy (dSTORM)), by using crafted laser emission signatures to temporarily deplete surrounding emissions (e.g. in Stimulated Emission Depletion (STED) [7]), or by decoding inference between repeated striping patterns (e.g. in structured illumination microscopy (SIM)), to name a few. The end result are localizations of fluorescently tagged structures or proteins at a precision below the diffraction limit, illustrated in Fig. 2-A. A relative straightforward multichannel SRM acquisition captures the channels sequentially, at the risk of inducing drift. More recently, parallel SRM acquisitions combine SRM mechanisms with spectral demixing algorithms to localize emissions with great accuracy in large numbers of channels [8]. The design of interaction analysis algorithms in multichannel SRM requires an appreciation of the sensitivity of these acquisitions. While exploring each modality in detail is out of scope here, we refer the interested reader to Lee et al.[4] and Rodriguez et al.[5].

### *1.2. The SRM triad: necessary compromises between spatial resolution, temporal resolution, and phototoxicity*

SRM acquisitions are determined by a compromise between three factors: spatial resolution, temporal resolution, and illumination. Spatial resolution is another term for the 'precision' in space, or the minimum observable distance $\delta_o$ between any two given objects, a function of the localization uncertainty $\epsilon$ of each object. Reconstructing complex and dense structures requires more localizations [9, 10] compared to simple homogeneous structures and thus higher spatial resolution. Increased localizations require more time, which, in turn, can reduce the temporal resolution, i.e., the minimum observable change over time. Higher illumination, by either modulation of laser power or length of exposure, can increase the number of photons the camera sensors observe, which is inversely squared to spatial precision (Section 3.2). However, illumination can compromise cellular health. Additionally, it can lead to early photobleaching, the decay of the fluorescence potential of the labelled targets. In short, there is a triad of factors that describe the unique compromising balance that each SRM acquisition must strike to optimize for specific use cases (Fig. 3).

### *1.3. Why not just use colocalization methods from diffraction-limited microscopy?*

The development of SRM specific interaction analysis methods emerged from the realization that the implicit model underlying 'colocalization metrics', such as Manders, Pearson, Jaccard, and others [11, 12], breaks down in SRM [13]. Colocalization metrics share the explicit assumption that the interacting objects are expected to share the same spatial coordinates, thus 'overlap'. However, the Pauli exclusion [14] principle states that no two particles can occupy the same spatial coordinates at the same time. In increasingly precise observations, such as SRM, it then becomes impossible for two objects to 'colocalize', breaking the principle of colocalization metrics for most use cases in SRM.

### *1.4. Interaction in SRM captures multiscale processes*

Here we describe the different scales, illustrated in Fig. 4, at which interactions take place below the diffraction limit. This division across scales has important consequences for interaction method design. First, *co-occurrence (I)* takes place when two labelled objects share the same physical space or are closer to each other than the precision of the system $\epsilon$. For example, labelling the same structure with different fluorescent markers or labelling two protein building blocks of a larger 'k-mer' are examples of cooccurrence. In SRM, this is the only instance where the term 'colocalization' is still applicable [15, 16].

Second, *adjacency (II)* occurs when objects interact at a distance of not more than 1-2 times the precision. Anchoring, fission, fusion, wrapping, and modular structures are relevant use cases.

Third, *proximity (III)* covers interactions at a distance from $\sim 2\times\epsilon$ to the diffraction limit. Examples are the spectrum of complex interaction ('contact') zones between Endoplasmic Reticulum (ER) and mitochondria with up to a dozen distinct proteins involved [17], or neurotransmission in the synapse [18].

Fourth, *topology (IV)* looks at the global spatial pattern of interacting objects using network and graph analysis algorithms. Type IV analysis can be leveraged to infer novel discovery on the underlying creation and destruction dynamics of protein

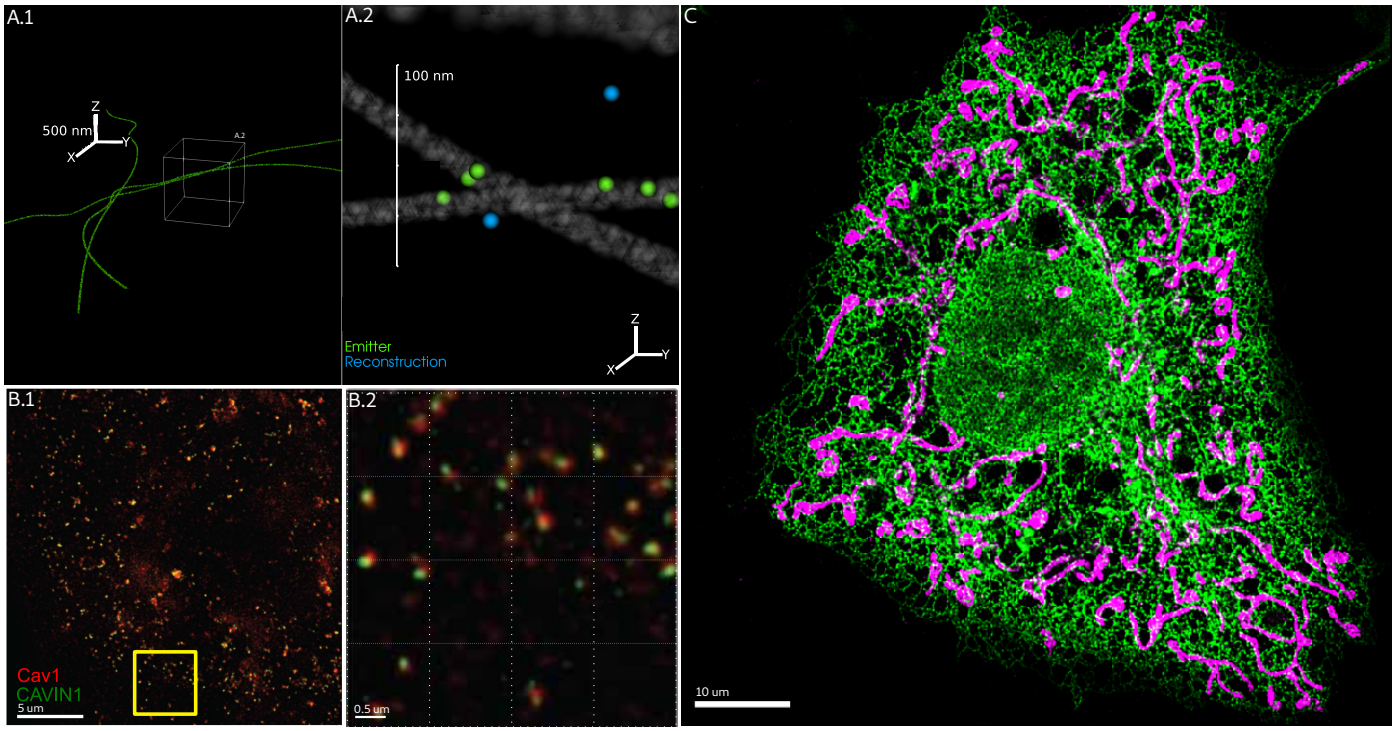


Figure 1: Illustration of the some SRM modalities in point cloud and voxel form. A1: 3D dSTORM of simulated microtubules. A2: Visualization of the distance between localization and source [1] in single channel SMLM highlights the impact on interaction analysis. Precision ($\epsilon$, Section 3.2): lateral ±10 nm, axial ±20 nm. B: 2D 2-channel STED microscopy of Cav1 (red) and CAVIN1 that form Caveolae [2], spherical ($\sim$ 100 nm) diameter invaginations in the cell membrane. Precision: lateral ±50 – 70 nm. Note that the precision differs between channels. C: 3D STED microscopy of ER (green) and mitochondria (magenta) [3]. Precision: lateral ±120 nm, axial ±250 nm. These are only a sample of voxel and point cloud based modalities, for an in-depth review of SRM modalities, we refer the interested reader to Lee et al.[4] and Rodriguez et al.[5]. Figures reused under author's original copyright.

structures, as well as inform equilibria modeling of the underlying processes. Topology can be a composite of any of the smaller-scale (I-III) interaction types.

Finally, when explicitly observed over time, interaction analysis is extended to temporal dynamics (V), focusing on change in interaction over time. Unlike topology (IV), where inferences on dynamics are made from static (2 or 3D) observations, here the input is a sequence of SRM acquisitions which each can contain interactions of type I to IV. Examples include 'particle tracking' [19], the task of recording a spatio-temporal trajectory per identified localization, and correlating those trajectories to infer visitation patterns. Temporal observation of localizations can sometimes be used to improve precision by resolving localizations to their emission source [20].

The stratification of sub-diffraction interaction scales is critical for method development. Capturing adjacency or co-occurrence can be done by density correlation-based methods, but at high precision such methods would fail to capture variable distance (III) accurately. In contrast, a proximity-oriented method (III) would not be able to differentiate between types I and II, where a density correlation-based method would be better suited. The review of methods (Section 5) shows a clear specialization of a given interaction method on a subset of scales (Table. 6), and allows the reader to review examples of each paradigm.

### *1.5. Existing reviews*

Our work was driven by an absence of recent comprehensive reviews of interaction analysis in multichannel superresolution microscopy. Here, we identify the closest reviews to contrast with ours, and identify reviews of adjacent topics of interest. Aaron et al.[15] and MacDonald et al.[21] highlight why confocal-based methods fall short for SRM-based interaction. In addition to the earlier identified issues with applying colocalization methods to SRM, they highlight that organelles can appear disconnected in SRM but not in confocal, and the marked increase in artifact-induced false positives and negatives. In their review paper, Wu et al.[22] reinforce the importance of quality control of Single Molecule Localization Microscopy (SMLM) [23] acquisitions, which parallels the recent work of Faklaris et al.[24] on quality control for diffraction limited microscopy. Khater et al.[25] discuss correlation-based multichannel cluster analysis, but omit voxel-based SRM multichannel interaction analysis, as do Hyun et al.[26]. Nieves et al.[27] propose a novel framework for validation, although omit multichannel SRM. Rodriguez et al.[5] review novel multichannel acquisition methods, but do not focus on analysis aspects. Lagache et al.[16] review colocalization methods, with a subsection dedicated to SMLM-derived methods. They stress the need for statistically inspired colocalization metrics, justified from the observation that SMLM data can be seen as localizations sampled from a Poisson process and thus need to be

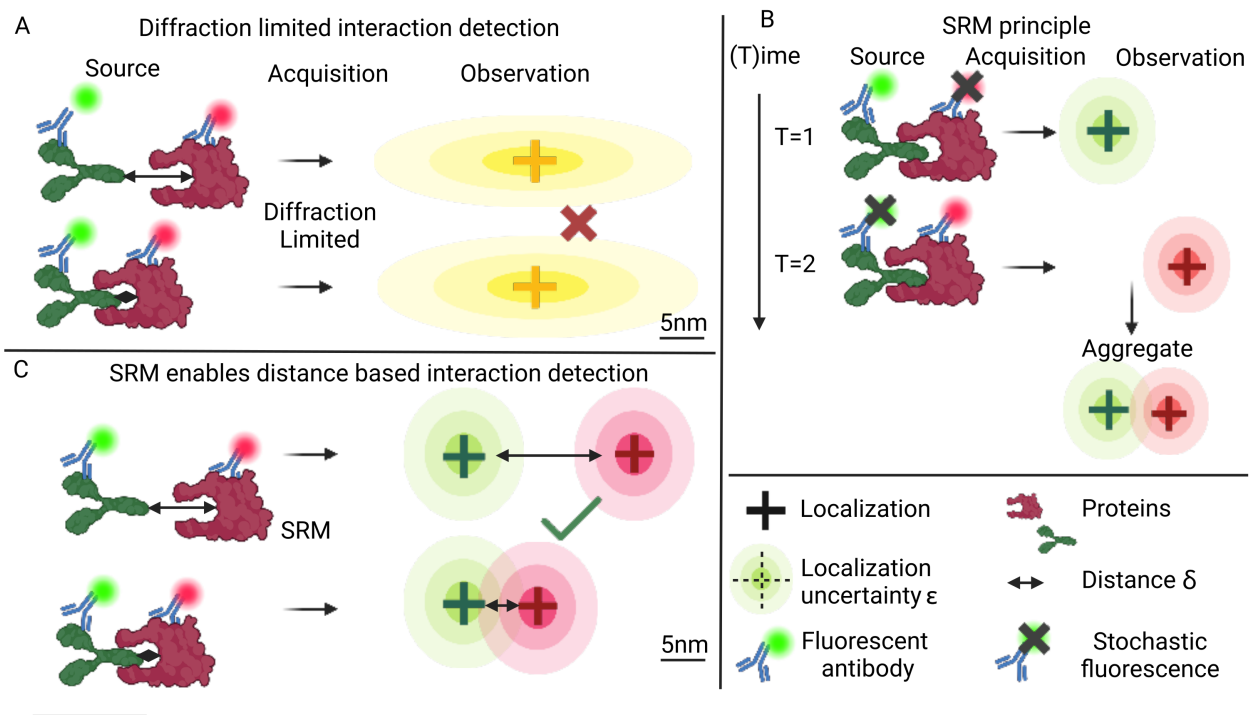


Figure 2: Illustration how SRM can enable more precise detection of interaction at the mesoscale. A: fluorescently marked proteins that are closer than the diffraction limit will be observed to co-localize regardless of their actual distance $\delta$. The observed distance cannot be distinguished from the minimum observable distance $\delta_o$, which is equal to the diffraction limit ($\sim$ 250 nm) B: SRM can use several mechanisms such as stochastic emissions or successive application of tuned laser patterns to name a few. In a multichannel setting, SRM channels can be acquired in sequence, or in parallel. In parallel acquisitions spectral demixing is frequently used to separate the superresolved emissions in different spectra. The common objective is to recover localizations with greater precision $\epsilon$ (Section 3.2, Eq. (15)). Here we show a simplified example of separating emissions in time through stochastic observations. Note that the fluorescent markers are recorded in separate channels. C: The much smaller localization uncertainty $\epsilon$ provided by SRM results in a minimum observable distance $\delta_o$ that is markedly lower than the diffraction limit. The resulting precision allows SRM to distinguish between different types of interaction at distances $\delta$ well below the diffraction limit. The observed distance in SRM is still an approximation of the actual distance, due to the added offset of the fluorescent marker and the non-zero precision of localization. For a complete overview of the different mechanisms behind the different SRM modalities we refer the interested reader to Lee et al.[4] and Rodriguez et al.[5] Image created in part using Biorender.com

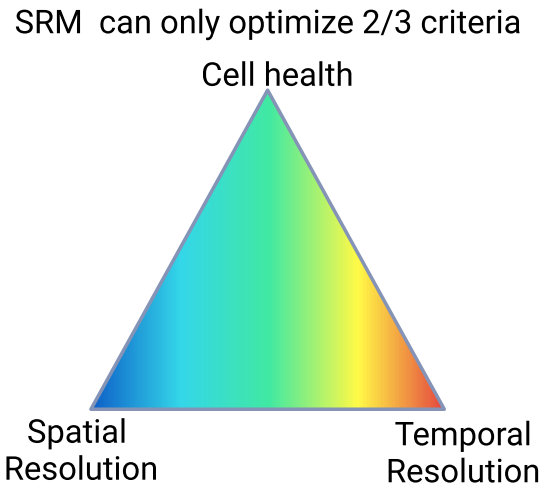


Figure 3: SRM acquisitions need to strike a balance between spatial resolution, temporal resolution, and cell health. Improving one dimension results in a compromise in another. For example, increasing spatial resolution can be achieved by increasing illumination by modulating laser power or the length of exposure. However, the increased illumination can adversely affect the cell in a way that can compromise cell health and function, and increase photobleaching. Increasing temporal resolution can be achieved by decreasing the time span during which localizations are captured, reducing spatial resolution. Each SRM modality finds a compromise in these three dimensions and often requires specialized interaction analysis methods for that use case (Section 1.2).

conditioned and contrasted against random colocalization effects.

Table 1: Overview of existing reviews in interaction analysis methods in superresolution microscopy and its adjacent topics. The most recent review that overlaps the most with our focus is highlighted in bold.

| Author | Topic |
|---|---|
| Lee et al., 2017 [4] | SRM acquisition and analysis |
| Rodriguez et al., 2022 [5] | Multichannel acquisition |
| Herce et al., 2013 [11] | Diffraction limited colocalization |
| **Aaron et al., 2018 [15]** | Colocalization methods in SMLM context |
| Hyun et al., 2023 [26] | SMLM clustering methods |
| Wu et al., 2020 [22] | SMLM analysis methods |
| Nieves et al., 2023 [27] | SMLM validation |
| Hansel et al., 2020 [28] | Biomaterial interaction in SMLM |
| Chenouard et al., 2014 [19] | Single particle tracking |
| Lagache et al., 2015 [16] | Statistical colocalization |
| Faklaris et al., 2022 [24] | Fluorescence microscopy quality control |
| Sage et al., 2019 [29] | SMLM localization algorithms |
| Saalfeld et al., 2022 [30] | Parallel optimized SRM storage formats |

### *1.6. Contribution, audience, and scope*

Given that recent reviews of interaction analysis in SRM have been absent, we here set out to:

- Provide a common mathematical framework through which existing and novel algorithms can be analyzed (Section 2).
- Identify superresolution specific factors that can compromise interaction analysis (Section 3).
- Review validation strategies for interaction analysis in SRM (Section 4).
- Identify, review, and discuss trends in novel interaction analysis algorithms (Section 5, Section 6).

## 2. A mathematical framework defining interaction in SRM.

Before we can discuss interaction analysis methods and factors that can compromise them, we first need to rigorously define the concepts of interaction, distance, and precision.

### *2.1. Defining interaction analysis as a multidimensional mapping*

In our review of interaction analysis methods Section 5, there was a noted absence of a formal mathematical problem statement of 'what' interaction analysis entails. In order to rectify this and enable a comprehensive comparison and analysis of methods, we introduce a mathematical framework based on all the studied art.

The interaction, observed by superresolution microscopy, can be modeled as a tuple of functions $<f, c>$, an interaction generation function, or mapping, $f$, and an associated confidence $c$. Each accepts a tuple of superresolution imaging data in a number of channels $C$ with spatio-temporal dimensions $D$ in voxel encoding (Eqn. 2) or point cloud (Eqn. 1) encoding. SRM data are observations ($Ob$) that measure the presence or absence of discrete biological structures at a given imprecise location:

$$Ob^D : \mathcal{H} \subset \mathbb{R}^D \rightarrow \mathcal{G} \subset \mathbb{R}^\eta. \tag{1}$$

Eq. (1) is a discrete ('point cloud') mapping of the $D$-dimensional subset $H$ of real valued coordinates to $\eta$-dimensional real valued metadata, such as localization precision, multiplicity, time, etc. An example of a protein structure at location $[0, 0, 0]$ ($D = 3$), localized three times with precision and frame number ($\eta = 2$) is given in Table 2. As a special case,

| $\mathcal{H}$ | $\mathcal{G}$ |
|---|---|
| $[0.2, 0.3, -0.2]$ | $[20, 1]$ |
| $[0.1, 1.3, 1.2]$ | $[17.5, 2]$ |
| $[-0.9, 2.3, 4.2]$ | $[22, 3]$ |

Table 2: Example SRM point cloud data in the mapping of Eq. (1), with $D = 3$, and $\eta = 2$. $H_i$ are the 3D coordinates (nm) of the localizations. $H_j$ are the empirical precision (nm, Section 3.2) and framenumber respectively.

SRM data can be captured by voxel-based representations:

$$V^D : \mathbb{N}^D \rightarrow \mathbb{R}^\eta, \tag{2}$$

where equispaced discrete coordinates in $D$ dimensions are mapped in a rectilinear array onto a range of either intensity or emission density or both in $\eta$ dimensions. Let $\theta$ be the hyperparameters of the interaction algorithm, $Q$ metadata of the acquisition such as precision, and CR the cardinality ratio (detailed in Section 2.2, Fig. 6). We can now construct our mapping for rectilinear data:

$$f_{\theta,Q,CR} :< V_1^D, ..., V_C^D > \rightarrow < V_1^E, ..., V_M^E >, \tag{3}$$

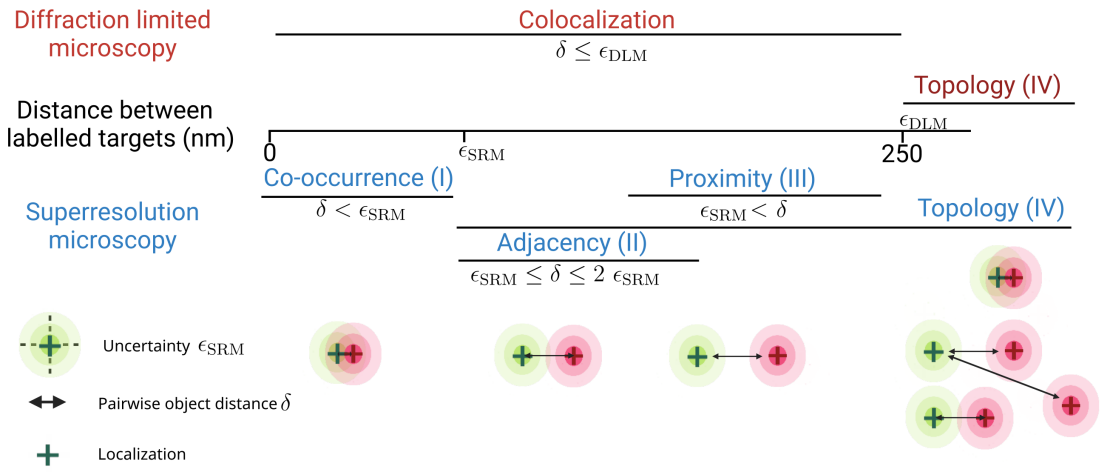


Figure 4: The multiple scales of interaction in SRM. A: Interactions between objects with distances $\delta$ between objects below the diffraction limit are covered by 'colocalization techniques in diffraction-limited microscopy. In SRM, however, there are four different scales of interaction informed by the diversity of biological use cases and the non-linear physics of scale (Section 1.4, Section 3.1). Each of the scales is graphically illustrated. $\epsilon$ refers to the 'precision' of the acquisition, for diffraction-limited this, depending on the wavelength used, is typically in the range of 250 nm. In SRM, $\epsilon$ is modality-specific but can be as small as 2 nm. Note that $\epsilon$ can vary between channels. See Section 3.2 for a more in-depth explanation of the actual computation of precision in SRM. Section 1.4 describes the different scales of interaction. Topology (IV), here, describes the spatial analysis of multiple objects with respect to each other, and as such spans multiple scales.

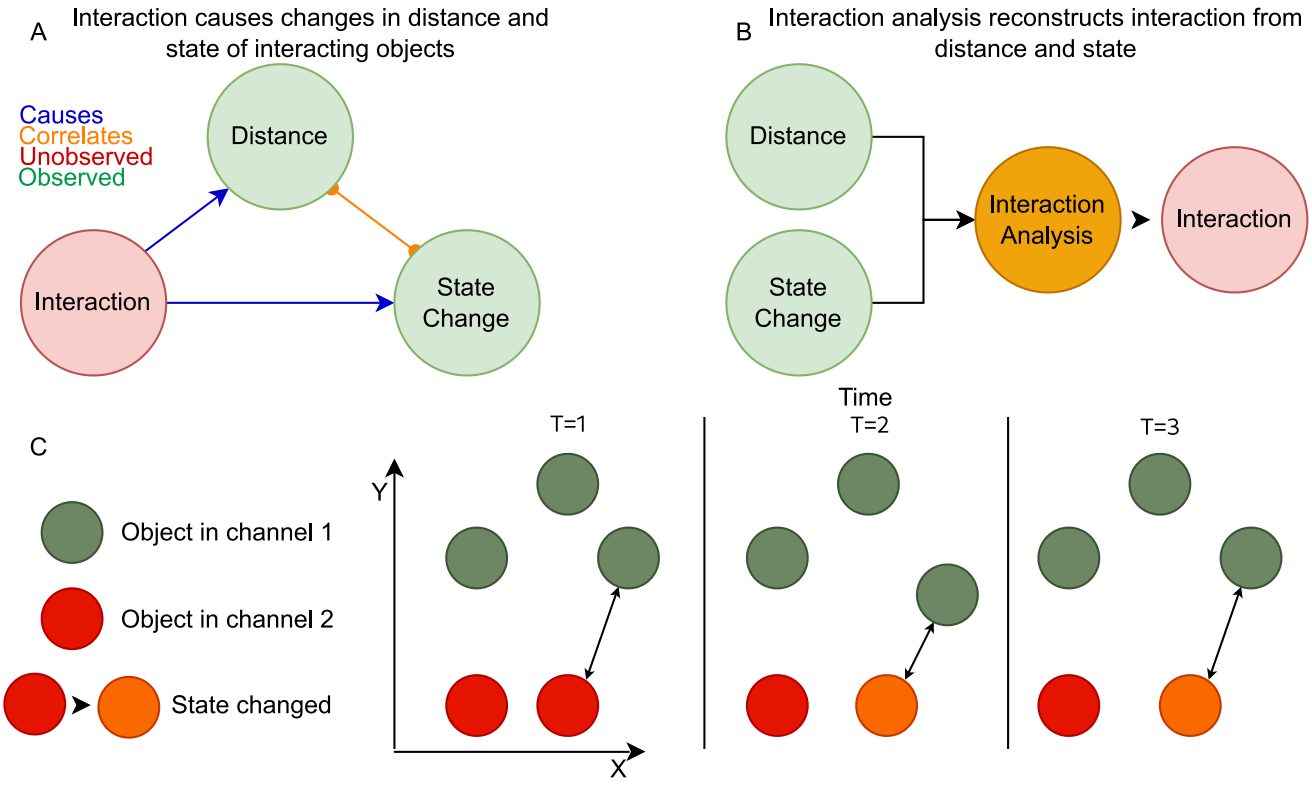


Figure 5: A: Interaction induces ('causes') changes in observed distance and state. B: Interaction analysis reconstructs the interaction from the observed changes in distance and state (Eq. (16)). C: Objects can be proximate but not change state, while interaction is characterized by a distance-mediated change in state (Section 3.8) This is illustrated by the red object changing state after proximity to the green object with which it is interacting.

where $C$ channels of in $D$ dimensions are input to the interaction function $f$, resulting in $M$ output channels in $E$ dimensions in rectilinear form. Rectilinear data with $D = 2$ would be referred to as 'pixels' and $D = 3$ 'voxels'. For point clouds, we have:

$$f_{\theta,Q,CR} :< P_1^D, ..., P_C^D > \quad \rightarrow \quad < P_1^E, ..., P_M^E >, \tag{4}$$

where $C$ is the number of input channels, $M$ the number of output channels, $D$ input dimensions, and $E$ output dimensions. The confidence function $c$, which is frequently paired with $f$, can be written, for example, for point clouds, as:

$$c_{f,\theta,Q,CR} :< P_1^D, ..., P_C^D > \quad \rightarrow \quad < P_1^E, ..., P_M^E > . \tag{5}$$

Examples of such a confidence function are the confidence estimates in computing distances between objects, 'p-values' or 'S-values' for statistics, and prediction confidence estimates for neural networks. It is equally possible to have a mapping from rectilinear to point cloud data and vice versa, for example visualizing 3D point cloud data in 2D pixel images.

### 2.2. Understanding the cardinality ratio (CR) of output to input

Given an interaction function $f$, CR($f$) is the ratio of the cardinality of the output to the cardinality of the input:

$$CR(f) = \frac{|y|}{|x|} \quad \forall f : x \rightarrow y. \tag{6}$$

Note that 'cardinality' here refers to the dimensions of the input and output at each function invocation, not the dimensionality of the domain and range (Eq. (1)). CR is an important characteristic in evaluating methods, as it captures the spatio-temporal extent of the interaction, and determines computational complexity of the interaction function. We can classify CR into three distinct cases:

$$CR(f) = \begin{cases} CR_{\uparrow}, & CR(f) > 1 \\ CR_{=}, & CR(f) = 1, \\ CR_{\downarrow}, & CR(f) < 1. \end{cases} \tag{7}$$

Examples of each case are illustrated in Fig. 6-A.2-4).

To demonstrate the complete notation introduced, let us describe the frequently used 2D pixel-based double channel correlation with a window size ($w$) of three ($\theta = \{w = 3\}$), applied to pixel based 2D STED with theoretical lateral precision of 100 nm ($Q = \{\epsilon_{XY}^t = 100 \text{ nm}\}$):

$$f_{\theta=\{w=3\},Q=\{\epsilon_{XY}^t=100\},SR_{\downarrow}} : \quad < V_1^2, V_2^2 > \quad \rightarrow \quad < V_3^2 >, \tag{8}$$

$$c_{f,\theta=\{w=3\},Q=\{\epsilon_{XY}^t=100\},SR_{\downarrow}} : \quad < V_1^2, V_2^2 > \quad \rightarrow \quad < V_4^2 > . \tag{9}$$

Eq. (9) is an accompanying 'significance' (c) function that gives, say, a 'p-value' for rejecting the hypothesis that correlation is due to random effects. Pairwise correlation has a range $V_3^2$ of [-1, 1], while probabilities have a range $V_4^2$ of [0, 1]. While the output has the same dimensionality as the input, the resulting correlation at the pixel coordinates $V_3[x, y]$ is a scalar (cardinality = 1), computed based on $V_{1,2}$[x-1, x, x+1, y-1, y, y+1] with cardinality 9, hence a compression operation ($CR_{\downarrow}$).

### 2.3. Order of interaction: symmetry meets h-arity

Common interaction analysis methods are pairwise, for example, two channels of input per output, yet data can consist of $C > 2$ channels. The 'h-arity' of a function describes the number of arguments that an interaction function accepts:

$$H : F \rightarrow \mathbb{N} : h = f(\langle V_1^D, .., V_h^D \rangle). \tag{10}$$

where $F$ is a family of functions. Let $\mathcal{P}_n$ be the ordered set of permutations of integers from 1 to $n$, with $\mathcal{P}_2 = \{(1, 2), (2, 1)\}$, and $\mathcal{P}_2[2] = (2, 1)$. Let $V_{\mathcal{P}_2[1]}$ be shorthand for the tuple $\langle V_1, V_2 \rangle$. The 'symmetry' $S$ of a function $f$ is defined as:

$$S(f) = \begin{cases} 1 & f(V_{\mathcal{P}_C[i]}) = f(V_{\mathcal{P}_C[j]}) \quad \forall i \neq j \in 1, .., C \\ 0 & \text{otherwise.} \end{cases} \tag{11}$$

For example, for two-channel twodimensional Pearson correlation $f(V_1^2, V_2^2) = f(V_2^2, V_1^2)$ and thus $S(f) = 1$. However, the distance between nearest neighbors is not symmetric. The 'order' $O$ of an interaction function $f$ is then computed with combinatoric notation as:

$$O(f) = \begin{cases} \binom{H(f)}{C} = \frac{H(f)!}{C!(H(f)-C)!}, & S(f) = 1 \\ \frac{H(f)!}{C!}, & S(f) = 0. \end{cases} \tag{12}$$

We illustrate this in Fig. 6-B 1-3.

Given that interaction is distance mediated, we now introduce distance between objects $i, j$ in channels $X_a, X_b$ at a time interval $[s, t)$ is then defined as:

$$d_{X_a,X_b}^{[s,t)}(i, j) : X_a \times X_b \rightarrow \mathbb{R}^+ : \|X_{a[s,t)}[i] - X_{b[s,t)}[j]\|, \tag{13}$$

where $X_{b[s,t)}[j]$ denotes object $j$ from channel $b$ observed between time $s$ and $t$. When time is omitted or not available, the shorthand $d_{X_a,X_b}(i, j) = d_{X_a,X_b}^{[0,+\infty)}(i, j)$ can be used. Distance between objects 'within' the same channels is denoted as $d_{X_a,X_a}(i, j)$. However, $d_{X_a,X_a}(i, i) \neq 0$, but $d_{X_a,X_a}(i, i) = \epsilon$. Each object's distance to itself can only be as small as the per-object localization uncertainty. $\|K\|$ denotes a context-appropriate norm of a vector $K$, ranging from the common L2 norm (Euclidean), $\|K\|_2 = \sqrt{\sum_{k \in K} k^2}$ ) to more refined measures that take into account location uncertainty and confounding effects such as anisotropy. We can now define objects in $X_a$ that are in proximity to those in $X_b$ within a distance interval $[\psi, \chi)$ at time $[s, t)$:

$$X_{a\,[s,t)}^{X_b}([\psi, \chi)) = \{x_i \in X_a \mid \forall x_j \in X_b \wedge \psi \leq d_{X_a,X_b}^{[s,t)}(i, j) < \chi\}. \tag{14}$$

For example, all objects in $X_a$ 'adjacent' to objects in $X_b$, with a localization precision $\epsilon$, at any time would be given by $X_a^{X_b}([0, 2\epsilon))$. The factor $2\epsilon$ stems from the observation that $\epsilon$ is a radius of uncertainty around a single localization, with adjacency involving two objects we need to account for double the radius. The set of objects at a distance in the interval [s, t) in $X_a$ is given by $X_a^{X_a} = X_a^{X_a}([s, t))$. We can now define empirical precision $\epsilon_e$:

$$\epsilon_e = \text{argmin}_{\delta} \mid |X_a^{X_a}([0, +\infty)) \setminus X_a^{X_a}([\delta, +\infty))| \wedge \delta > 0. \tag{15}$$

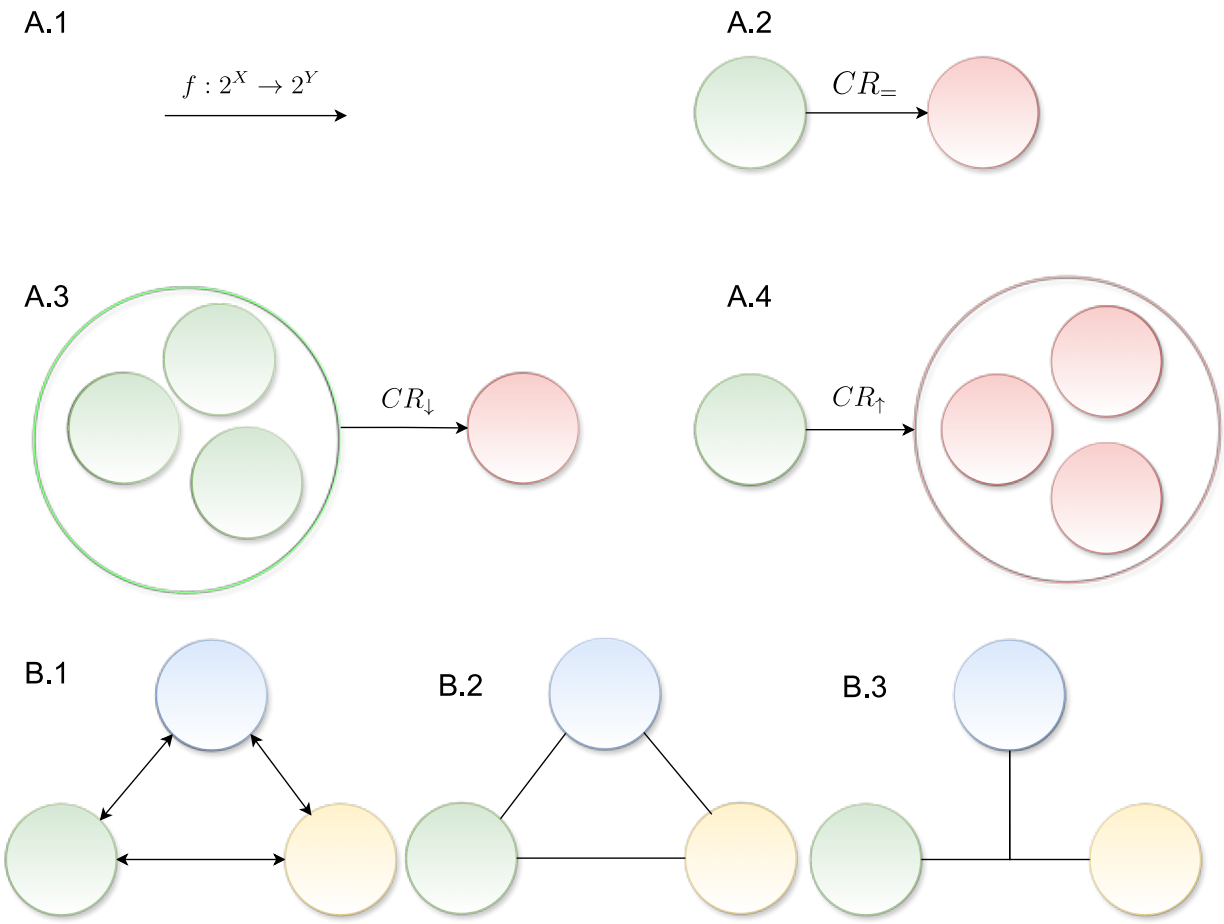


Figure 6: Graphical illustration of the concepts of CR (Section 2.2) and 'order' (Section 2.3) for interaction functions. A: CR of an interaction $f$ describes spatial extent of the interaction (Eq. (6), Eq. (7)). Examples: nearest-neighbour distance ($CR_=$, A.2), windowed correlation ($CR_\uparrow$, A.3), k-nearest neighbour ($CR_\downarrow$, A.4). B: The 'order' describes the way in which the number of interacting channels is combined in the context of their symmetry. From left to right: nearest neighbour distance is a directed pairwise example, density correlation is an undirected pairwise example, while overlap of three channels could be an example undirected three-way interaction. The order (Section 2.3, Eq. (12)) of the examples is given by B.1: $\frac{2!}{3!} = 6$, B.2: $\binom{2}{3} = 3$, B.3: $\binom{3}{3} = 1$.

| Scale | Definition |
|---|---|
| I | $X_a^{X_b}([0, \epsilon))$ |
| II | $X_a^{X_b}([\epsilon, 2\epsilon))$ |
| III | $X_a^{X_b}([\epsilon, \epsilon_{DLM}))$ |
| IV | $X_a^{X_b}([\epsilon, +\infty))$ |

Table 3: Interaction scales in SRM defined using mathematical notation between objects in two channels. (For notation definition and concepts, see Section 1.4, Fig. 4, Eq. (14)).

In other words, $\epsilon_e$ is the smallest distance that can be distinguished from zero in the pairwise distance distribution between objects in channel $a$, in the data. It is important to note that $\epsilon_e$ describes uncertainty 'within' a single channel. In general, the empirical precision is higher ('worse') than the theoretical precision: $\epsilon_e \geq \epsilon_t$ (Section 3.2). Even if for all localizations $\epsilon_e = \epsilon_t$, if those localizations serve to reconstruct a complex object, due to undersampling [10, 9] the empirical precision of the structure can still be compromised: $\epsilon_e > \epsilon_t$. Finally, the precision 'across' channels is a complex function of the uncertainty and empirical precision per object, per channel. The introduced notation allows us to distinguish between the 'scales' of interaction (Section 1.4, Fig. 4).

### 2.4. *Inferring interaction from differential change in distance and state*

We now have a sufficiently complete notation to define interaction as the change in the observed distance and state $Q$ over time $t$. 'Interacting' objects below the mesoscale with diffraction limit $d_l$ are then those objects whose state changes markedly over time when proximate, compared to all objects independent of proximity:

$$\frac{dQ(X_a^{X_b}([0, d_l))}{dt} >> \frac{dQ(X_a^{X_b})}{dt}. \tag{16}$$

The notation >> stands for 'markedly larger than', which in practice can be a significance test, threshold, or confidence value. Figure 5-C illustrates the definition. The interaction methods studied here approximate the above differential function either implicitly or explicitly. Even if the data studied are observed without an explicit temporal dimension, it is still feasible to identify interacting objects because the observations essentially capture a *snapshot* of objects in various stages of interaction [31].

## 3. Factors that compromise interaction analysis

Here we review factors that methods have to take into account in order to accurately reconstruct interaction.

### 3.1. *The non-linear relation between energy and distance at the mesoscale*

Distance implicitly measures the energy required to bridge a spatial gap between any two objects in the cell so that they can interact. Human perception of distances tends to be linear: the energy required to walk one kilometer is, all else being equal, double the energy needed to walk 500 m. However, doubling the distance on the mesoscale [32] does not necessarily imply doubling the required energy. This is indicated by the Reynolds [33] number, describing the balance between momentum and inertia in moving objects, which at the mesoscale is markedly different [34]. Correctly modelling this is therefore of great importance in interaction analysis.

### 3.2. *Factors that determine precision in SRM*

Precision directly affects the estimation of distances between objects and the ability to group or segment objects. The precision in diffraction-limited microscopy is, given numerical aperture (NA) = $\sin\theta$, and wavelength ($\lambda$) of the light, determined by Abbe's limit of the minimum observable distance $d$:

$$d = \frac{\lambda}{2\text{NA}}. \tag{17}$$

Related to this is the full-width half-maximum (FWHM) criterion of a fluorescence emission $f$ point spread function (PSF):

$$FWHM(f) = 2k \mid f(x-k) = f(x+k) = \frac{\max(f(x)\ \forall x \in X)}{2}. \tag{18}$$

Two objects can now be considered distinct as long as their respective intensity profiles do not overlap at or above the FWHM. However, the FWHM relies on the assumption of isotropic symmetric intensity profiles. In SRM, however, precision is a much more complex criterion. Here, we review SRM-specific factors that can determine precision in interaction analysis.

#### 3.2.1. *Empirical versus theoretical precision*

Theoretical precision quantifies the 'best-case' or 'average-case' precision of an acquisition, based on a simplified model of the optics and reconstruction algorithm. Theoretical precision itself is bounded by the Fréchet-Darmois-Cramér-Rao lower bound (CRLB) [38] theorem which specifies the maximum possible precision, given specific conditions such as PSF and localization model. Empirical precision (Eqn.15) is the actual precision per localization or per voxel. The difference between them is often large because density, noise, drift, localization, multiple blinking, and any number of other subtle factors conspire to degrade actual precision, while theoretical precision relies on simplified assumptions and PSF related modelling. Although theoretical precision is informative, empirical precision is more important for interaction analysis methods, as it is more accurate, as illustrated by its leverage in recent methods [39, 40]. The Fourier ring correlation (FRC) [41], frequently used in EM to estimate empirical precision, is often used in SMLM. Critically, Van Heel et al.[42] noted that a replicated error slipped in the recommendation on its usage, with widespread unobserved errors in years of publications. This underscores how important it is not only to estimate but also to understand precision-based effects. Thompson et al.[43] derive that, for SMLM, the localization precision of a single emission with photon count

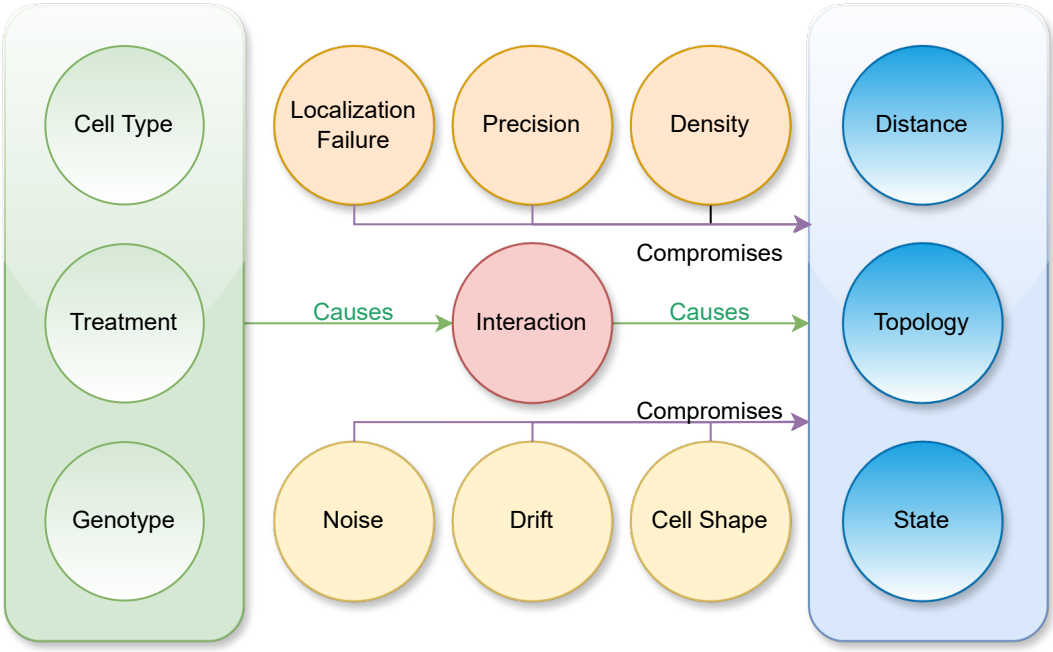


Figure 7: Compromising factors in interaction analysis (Section 3). Biological factors such as cell type, treatment, and genotype directly control the interaction in the cell. The interaction is indirectly observed by changes in distance, state, and topology. However, compromising factors ranging from noise, precision, and drift to more SRM specific factors such as density and localization failures can bias interaction analysis.

$N$ is bounded by $\frac{1}{\sqrt{N}}$ for high photon count events, and $\frac{1}{N}$ for low photon count events where background becomes more of a problem. This landmark paper is the reason why the empirical precision in SMLM is often referenced as 'Thompson precision'. More recently, Endelsfelder et al.[44] derive precision as interaction (NeNa) [20], an empirical precision estimate without thresholding or reliance on FRC. Mazidi et al.[45] adapted an empirical precision measure specifically tuned towards protein structural heterogeneity. He et al.[46] published a detailed evaluation of empirical precision in minimal photon fluxes (MINFLUX), one of the most precise SMLM modalities to date. For the effects of chosen or fitted PSF models on precision, see Siemons et al.[47] and Coles et al.[48].

### 3.3. Bleedthrough: false positives induced by anisotropy.

'Bleedthrough' refers to an effect where the phantom intensity is present several hundred nanometers away from its source, leading to false positives in interaction analysis. For example, in 3D anisotropic STED, at Z-slice k, one can observe intensity profiles from bright emissions at slice k±5, 500 nm away from its source [3]. Because the precision and PSF of 3D STED is anisotropic, the effect is stronger in the axial direction than in the lateral direction. An interaction analysis method that does not have corrections for these effects can introduce phantom interactions where actual physical objects do not interact. For interaction analysis, cross-channel bleedthrough is equally important. With the increasing number of channels and a limited fluorescence emission spectrum, novel PSF engineering is needed to minimize this.

### 3.4. Wobble Effect: Unexpected lateral anisotropic localization error

As one moves away from the focal plane, precision degrades, but less well known is that this degradation is *not* necessarily the same in X as it is in the Y axes. The term 'wobble' refers to the fact that if one visualizes or plots the precision, this anisotropy in precision creates an optical wobble effect [36]. Let $\epsilon_X[x]$ and $\epsilon_Y[y]$ be the localization error or uncertainty at the location $x, y$ on the X and Y axes, respectively. As one moves away from the focal plane along the X/Y diagonal, the precision in localization in the x and y coordinates, represented by the expected error, is expected to increase (Fig. 8-B.3.1). Less well known is that the error can diverge (Fig. 8-B.3.2):

$$\lim_{q \to \min(X,Y)} \|\epsilon_X[q] - \epsilon_Y[q]\|_2 \to k \;\; |k > \epsilon, k \in \mathbb{R}^+, \tag{19}$$

with $k$ reaching in the order of several dozen nanometers in severe cases.

#### 3.4.1. Anisotropic precision

Because lateral precision is a linear function of the NA, whereas the axial precision is quadratic in NA, precision in SRM is frequently worse axially than it is lateral, inducing anisotropy. Empirically estimation of the lateral precision can be done using multiple increasingly separated objects, such as a grid of beads in the lateral plane with increasing known separation; this is much harder to do in the axial plane. To empirically estimate the axial precision, the FWHM (Eq. 18) criterion is sometimes used instead.

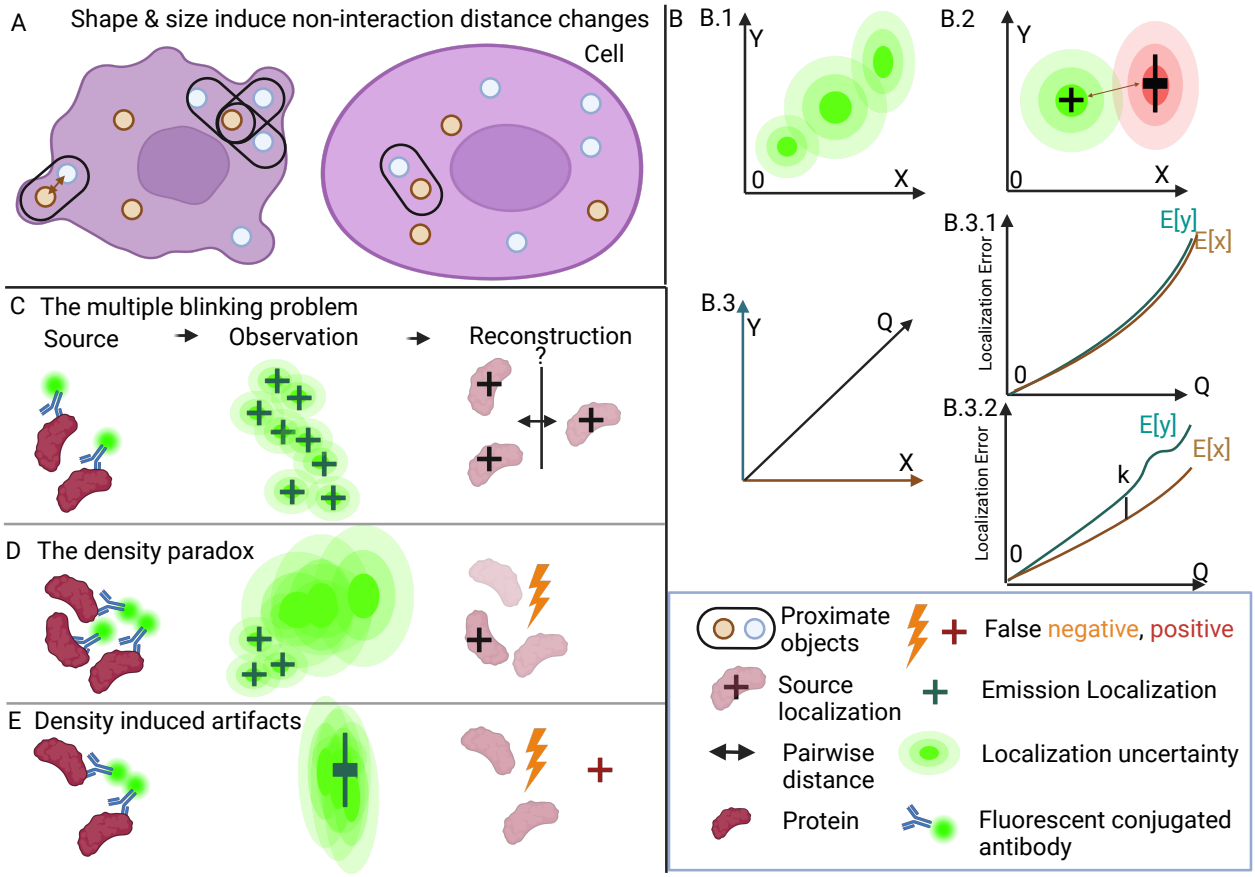


Figure 8: Illustration of SRM factors that can compromise interaction analysis. A: Cell shape and size can change the proximity (pairwise distance) between objects [35]. However, the observed differences in proximity do not necessarily reflect interaction-induced changes. Therefore, interaction analysis methods that rely solely on distance should contrast with the expected proximity, given the size of the objects and the configuration of the cell shape [35]. B: The localization precision is variable (B.1) and can be both anisotropic and differ between channels (B.2) The anisotropic deformation of the localizations across channels and axes is illustrated by elongation in Y for red, where this isotropic for green. B.3: The localization error is expected to degrade as the distance to the center of the focal plane (Q, B.3) increases (B.3.1). What is unexpected in the lateral plane is that the error deviates between the axes, referenced as the 'Wobble effect' (B.3.2) [36] (Section 3.4). Distance-based interaction methods should take advantage of distance functions that are adapted to these effects. C: Mapping localizations to their source is named the 'multiple blinking problem', 'particle averaging', 'particle fusion', or 'merging'; a nontrivial inverse problem that is still an avenue of active research. D: The high density of emissions can lead to a critical failure in localizations: the 'density paradox' [37]. The density of proximate emissions compromises the spatio-temporal separation principle, leading to localizations with unacceptably high errors, which are removed from the final output. The result can be a local zone of false negatives where the structures are not localized at all. E: High density of proximate observations can be observed as a joint point spread function with anisotropic configuration in X/Y. This can induce a combination of false negative and false positive in astigmatic SMLM [1]. Astigmatic SMLM relies on the anisotropy of the observed intensity to induce a third spatial axis. Density can lead to falsely superimposed anisotropy, leading to a false negative *and* false positive. All of these effects can compromise interaction analysis. Image created using BioRender.com

### 3.5. Drift, registration, and tracking

SRM acquisitions are often captured over time, leading to time-dependent spatial variations, referred to as 'drift'. Drift correction is the process of reversing this temporal offset, which can lead to errors of 100 nm and more. A common strategy is to insert metallic spheres, 'beads' or 'fiducials', that are recognizable by the fact that they fluoresce nonstop, in contrast to stochastic emitters. Fiducials can then be used in postprocessing or in real time [49] to allow the inverse correction. Fiducial free methods exist using deep learning [50], cross-correlation [51], Bayesian models [52] , entropy minimization [53], and advances in generative learning [54]. Nonetheless, resolving drift in multichannel SRM remains an open complex problem [55] because the interaction is unknown and therefore difficult to isolate and preserve from the drift correction.

### 3.6. Density based effects

In this section, we review how labeling and localization density can become compromising factors. First, in astigmatic dSTORM, where an astigmatic PSF is used to recover depth, the presence of multiple proximate emissions can cause a similar mislocalization of a phantom several 100 nanometers beyond the actual object, with potentially disastrous effects for analysis. Recent work uses deep learning [1] and wavelets [56] to correct for this during localization.

Second, in SRM each emission source results in multiple localizations. Mapping the localizations to their corresponding source locations is an ill-posed inverse problem, referred to in the literature as the 'multiple blinking problem' (Fig. 8-C). The ill-posed nature is in part due to the fact that source locations can be closer to each other than their corresponding localizations, making it under-determined to decide, for each localization, what its source was. The search terms 'particle averaging' [57] and 'particle fusion' [58] are also used in the field, as is the unfortunately overloaded term 'registration'.

The physical process that generates localizations from observations of emission sources is often approximated as a Gaussian. The inverse problem of assigning $K$ localizations to $M$ sources ($K \neq M$) can then be modelled as a Gaussian mixture model [59] or an implicitly learned model [60]. Recently, Wang et al.[58] combined random initialisation and Bhattarachaya distance to avoid local optima in this process to achieve much improved results and improved empirical precision. Although such methods are often benchmarked on phantom structures with high symmetry, recent work is now exploring performance on heterogeneous structures [61, 45]. There are also model-free or template-free approaches that group emissions based on distance thresholds [62]. Solving the multiple blinking problem is often a first step before clustering the resulting point clouds [25].

Third, in SRM and specifically in SMLM, the density can become so high that the localization algorithm fails because the spatiotemporal separation principle is compromised. The resulting image will then show an increasingly bright emission in confocal, but its SRM-paired image will show a region with a paradoxical absence of localizations where intensity should be highest [37] (Fig. 8-D). Both detection and prevention of these artifacts are open problems in SRM[63, 64], but in multichannel it can introduce more false negatives that affect interaction analysis.

### 3.7. Noise

Noise is a subset of the observed acquisition that is not informative. Here we will describe how SRM specific noise can compromise interaction analysis, as is evident from the frequent use of clustering algorithms that are designed to be noise resistant [65, 66, 67].

#### 3.7.1. Acquisition noise

Chai et al.[68] show in a careful evaluation of convolutional neural network (CNN) based segmentation networks that such segmentation is highly sensitive to changes in signal to noise ratio (SNR), with the average segmentation border error increasing rapidly beyond 1-2 pixels for each decrease in SNR. Two problems then arise. First, the SNR is not going to be identical across channels, so an implicit bias is now induced. Second, use cases, such as interaction between organelles, can require a precision that would need an unbiased segmentation error of at most 1/10th of a pixel in order to accurately capture the subpixel distances [3]. In interaction methods, denoising is often done in real data by selecting an ROI outside the cell [69], and designating those data as a typical model for acquisition noise. In simulated point cloud data, the uniform distribution of sparse localizations is frequently used, whereas in voxel-based data the joint Poisson-Gaussian additive noise model is common, although recently a deep learning-based approach trained on Perlin noise was proposed [70].

#### 3.7.2. Semantic noise: excluding the non-informative

Semantic noise, unlike acquisition noise, is derived from observations of biophysical origin, but is explicitly *not* the target of the experiment. Costello et al.[64] enumerate SMLM specific artifacts that can bias downstream analysis methods. A striking example is a localization failure induced sparsity that appears as a 'sharpening' in the visualized point-cloud data, misleading an unexpected end user to mistake the data for high precision localization. Another example is self-organized labelling [71] appearing as distinct observations with intensity above background noise thresholds. A robust way to detect and remove these can be to train a model in a cell where the expression of the target protein is genetically disabled, so only nonspecific labelling will be present [2]. A final example is the recently reported effect that fixation, a common process in the preparation of cells for imaging, can induce artificial effects [72].

### 3.8. Distance distribution effects: distinguishing interaction from random proximity

Distance-mediated interaction analysis works from the assumption that interaction causes a change in observed distance. However, first shown in confocal microscopy [73], the distance

observed between two objects can be the result of the size and shape of the cell, the location of the object and the relative density of proximate objects, and the size of the object. It is critical to distinguish between interaction-induced distance observations and the expected distance between any two objects in the cell (Fig. 8-A, B). This can be done by randomization experiments to compute the expected distance distribution due to spatial factors alone [73], or by deriving closed form equations [35] for the probability of colocalization in SMLM given the shape and size of the cell and the size of the objects in question. A related effect is sometimes referred to in interaction method design as 'edge effects' [69] (Fig. 8-B). An object located at the periphery of the cell has restricted space for interaction compared to objects in the unrestricted center. Edge effects are one reason why triangulation-based methods often prefer tesselation [74, 66] over Delaunay triangulation to avoid such effects.

### *3.9. Acquisition, localization, and algorithm parameters*

The optical, chemical, physical, and computational methods that enable SRM acquisitions are encumbered by complex parameter spaces. The complexity increases with multi-channel acquisitions and with it the risk that interaction observations are due to channel-dependent tuning, rather than actual biology. To tackle this, public reference configurations [75], machine learning-based optimization [76, 77], and expert guidelines [24] have been proposed. One parameter of special interest for interaction analysis is the voxel dimension configuration. According to the Nyquist-Shannon-Whittaker [9, 10] theorem, the dimensions of the voxel are to be set as a function of theoretical or empirical precision, which in turn varies across channels. The resulting difference across channels can lead to aliasing, over- and undersampling, misalignment, and estimation errors in cross-channel distance computation.

## 4. Validation strategies in interaction analysis

In this section we document how interaction analysis methods are validated and why that can be challenging given the sparsity of ground truth [32].

### *4.1. Validation with ground truth data*

Ground truth sources can be simulated ('in silico'), phantom, or real-world data. Simulated data is generated by either generative learning or complex simulation algorithms that approximate an SRM acquisition from protein structure all the way up to optics, localization, and reconstruction [88, 89]. Phantom data are acquisitions in which artificial objects are introduced with known characteristics, for example, DNA origami [90], fluorescent beads, or even simply by only capturing background labelling [2]. A hybrid form of phantom data is the separated or split fluorescent probe (SFP) [91] that only fluoresces when the separated parts come together. Two distinct objects are labelled by one part of an SFP; each will then fluoresce only where the two objects are proximate enough for the SFP to reassemble. Real data are actual acquisitions of cells where the interaction is known to be present, optionally associated with specific markers or expert annotations. A prime example of real-world ground truth data are nuclear pores [92]. Due to their well-documented structure and simple geometry, nuclear pores can be leveraged to calibrate acquisitions, including across multiple channels. A common strategy is labelling the same structure with two independent markers, for example, microtubules [93, 39], to detect if Type I (co-occurrence) interaction is detected and to what extent. In DNA-based studies, prior knowledge of known chromatin co-occurrence is leveraged to validate Type I focused methods [13, 94, 95, 67]. However, care must be taken not to overfit on real world data that can lack diversity and heterogeneity.

The level of detail of the ground truth determines if the validation can be performed on a per-pixel or point, structure, or at higher aggregated levels all the way to cell- or image-level labels only. The finest level of detail is rarely, if ever, available in real-world data. The next level is the region-based detail, where phantom data such as DNA origami [96] and SFP can be used. If only cell-level data are available, such as culture, cell type, treatment, and genotype, interaction analysis validation is now restricted to methods from the weakly supervised paradigm. Common examples are Type II-III interactions, such as ER-Mitochondria contacts [97, 3] or synapse studies [98]. An example of weak label validation in Type I-II interaction is demonstrated by LAT-modulation (Linker for ac-

Table 4: Overview table of reference works that describe causes and remediation of compromising factors in multichannel interaction analysis in SRM, together with reviews on adjacent topics in SRM multichannel analysis.

| References | Topic |
|---|---|
| [78, 79] | Imbalanced data |
| [56, 1] | Artefact removal in SMLM |
| [77] | Hyper-parameter optimization |
| [47] | Axial anisotropy |
| [80, 81] | Point cloud to image visualization in SMLM |
| [48] | Optical aberration |
| [68] | Sensitivity of CNN based segmentation |
| [21] | Confounding factors in SRM |
| [64, 63] | SMLM-specific artifacts |
| [82] | Probability distance functions |
| [46] | Empirical precision in MINFLUX |
| [43, 20] [45] | Empirical precision in SMLM |
| [83, 84] | Theoretical precision in SMLM |
| [50, 53] [85, 55, 51] [52, 54] | Drift correction and multichannel registration in SMLM |
| [37] | Density paradox in SMLM |
| [42] [86] | FRC and empirical precision in EM |
| [43, 83] [84] | Theoretical precision in SMLM |
| [36] | 'Wobble' effect - anisotropic lateral precision in SMLM |
| [57, 58] [59, 60] | Multiple blinking/particle averaging/fusion/'registration' |
| [87] | Adaptive image formats for large SRM data |

tivation of T cells [99]) as seen in Baragilly et al.[100], where LAT-modulation controls direct interaction with T-cells.

### 4.2. Imbalanced results: attention to detail

Imaging cell biology in SRM often results in a snapshot of highly complex processes that may not yet have converged to an equilibrium, resulting in distributions that are heavily skewed or long-tailed [101]. Thus, validation must be designed in a way that is robust to long-tail data. For example, in the case of aggregate values, care should be taken to understand the possible confounding effect of outliers [79] or extreme values [78]. The presence of edge effects almost guarantees imbalanced data if object interaction is measured across the cell. A frequent mitigation strategy is often to restrict the data to expert-selected ROIs [74] or to contrast the outcome of the interaction between cells [97]. Approaches such as Heinrich et al. [102] first segment different organelles, then establish interaction. However, the segmentation performance of each individual organelle differs dramatically, potentially compromising the results. SRM segmentation performance is rarely evaluation in a multichannel environment. High performance in one channel does not guarantee high performance in another, compromising segmentation-based interaction analysis. For example, the interaction between mitochondria and ER, acquired in 3D STED, is distinguished between cell types by a difference in mitochondria coverage of 3-5% [3], with a total coverage ranging from 5-12% in a volume of 2000x2000x70 voxels. Pixel-level ground truth is not available for supervised segmentation training or validation of semi- or unsupervised methods. Segmentation of the ER is still an open problem. To capture this type of interaction accurately by segmentation, 3D segmentation would need to have a per-pixel accuracy greater than 97.5%, in each channel, consistently across SNR variation. Yet Chai et al.[68] show that state of the art segmentation in microscopy demonstrates a boundary error that, on average, increases by 1 pixel for every decrease in SNR. Critical for interaction, SNR is rarely the same across channels or cells. This resulted in alternative approaches, such as deep learning generative methods that are explicitly designed to be fair in their multichannel segmentation targets [103] or segmentation-free approaches [3] (Section 5.1).

### 4.3. Using other methods as validation

A special case of validation occurs when a method is introduced to improve previously published methods. A novel direction here is the mathematical quantification of 'conflict' or 'disagreement' between statistical models with techniques from fuzzy computing [104], recently applied to 2D STED SRM [2]. Typical scenarios in cross-method validation can be specializing towards specific use cases [74], optimizing for memory or runtime [40], or reducing parameter complexity. The genealogy tree in Fig. 9 and Table 6 shows a low out-degree, meaning a method has few descendants or methods that improve on it. Some of the reasons for this are the relative absence of diverse benchmark datasets, reproducibility, and specialization to specific interaction scales and use cases (Fig. 4).

### 4.4. Multi-modal validation

Multimodal validation uses different modalities on the same biological specimen to confirm or compare the results. This can be a powerful validation strategy, as it can isolate acquisition problems from the interaction results (Section 3). Multimodal validation is expected to show to practitioners strong evidence of interaction in a biological specimen in two or more modalities. For example, EM 2D ROIs can partially confirm the presence of interaction, or Western blot tests can roughly confirm by antibody response the relative presence or absence of targeted proteins.

Validation by modalities with higher precision, such as EM, is not always feasible. First, in EM, it is more complex to label individual proteins that can be distinguished by distinct markers in fluorescence-based modalities. Second, EM-based validation of fluorescence microscopy requires that the modalities need to be registered, which is nontrivial. Third, EM requires irradiation and invasive preparation of the cell, ruling it out for use cases where SRM can still be applied. For those SRM specific cases, validation by EM is then not possible. A hybrid form is correlative light electron microscopy (CLEM) [105], where EM and light microscopy are applied to the same region, solving some of the aforementioned issues. In other words, the modality bridges otherwise separated scales of validation.

### 4.5. Stability and robustness enable end user trust

The presence of SRM specific artifacts and noise [63, 1, 64, 37] results in a strong focus [106] on 'stability' and 'robustness' of interaction in the presence of such factors. Stability is the property of a function $f$ to change the output only in a bounded way in response to a corrupting function $h$ applied to its input: $\exists\, \chi \in \mathbb{R} : \|f(I) - f(h_\chi(I))\| < \psi$ with $\psi$ sufficiently small, where $\|A - B\|$ denotes a norm, frequently the L2-norm. For example, uniform additive noise could be modeled as: $h$: $\exists\, \chi \in \mathbb{R} : \|f(I) - f(I + \chi)\| < \psi$, the function $f$ would be 'unstable' if $\psi$ grows unbounded or unpredictably as a function of changes in $\chi$. More formally, the limit in Eq. (20) diverges.

$$\lim_{\chi \to +\infty} \frac{\|f(I) - f(I + \chi)\|}{\psi} \tag{20}$$

The problem is that this stability is often tested with the assumption of additive noise, which is a particularly incomplete noise model in SRM [37, 71, 63]. The density paradox (Fig. 8-D) is a counterexample of destructive multiplicative noise [37].

### 4.6. Robustness minimizes practitioner surprise

The related concept of 'robustness' minimizes end-user surprise when applying a method to new data. It is defined by the entropy of the change in a function when changing datasets. For a statistical test with significance $p_s$ the 'surprise' (S) value [107] is the Shannon entropy encoded in the significance of comparing two distributions:

$$S(X, Y) = -\log_2 p_s(X, Y). \tag{21}$$

If $f$ is an interaction analysis method, we can then express robustness as the 'surprise' or the unexpected change in output on different datasets $\mathbb{I}$ that acquire the same biological specimen:

$$R_f = \frac{1}{\mathbb{E}[S(f(I), f(J))]} \quad I, J \in \mathbb{I}. \tag{22}$$

While the underlying specimen does not change, the acquisition signature, such as intensity and density, and compromising factors such as cell shape can change, inducing unexpected changes in the output of the interaction analysis method. An example of this is overfitting to benchmark phantom data, recently illustrated by Huijben et al.[61] in the reconstruction of heterogeneous structures. The frequent use of structures that exhibit high structural symmetry and homogeneity, such as microtubules [108, 74] and nanopores [109] is understandable in method design, but can compromise robustness by overfitting to these more straightforward cases, hiding potential issues with more complex use cases where discovery is still an open problem [97, 110]. Statistical or model-based methods focus on a 'chain of evidence' or interpretability by design, to ensure robustness. For example, methods that contrast observed distances against the probability of random distances are an example [35, 111, 112](Fig. 8-A, B). An alternative approach is to leverage a statistical model [100, 113] designed to address factors that compromise robustness.

### *4.7. Robustness across replicates and parameters*

While it is expected to have consistency within a replicate, an independent repeated experiment, but across replicates in intensity, precision, expression, can compromise analysis. Although often quantified and then compensated for, it is more optimal to have methods that automatically adapt to this variance. Adler et al.[114] show one way of adjusting Pearson-based colocalization metrics by computing the expected value of replicate-wise variance, and scaling the results by this value. Methods from single cell genomics [115] to mitigate the similar batch-based effects can be ported to enable replicate consistent SRM interaction analysis. However, optimizing for consistency without taking into account the fact that some replicates can fail or be weak indicators risks compromising the method's design.

### *4.8. Qualitative analysis: seeing is not always believing*

Qualitative analysis in interaction analysis is based on the fidelity of visualization of SRM data. Here, we review factors that can unexpectedly induce implicit bias by visualizing SRM data and potentially compromise discovery [116]. First, mapping channels to colors such as RGB images is problematic, as human color sensitivity is highly personal [117]. In addition, reliance on such color mapping can be non-inclusive for colorblind readers. Reliance on grayscale representation is also not a solution, as grayscale perception is much more limited in humans [118, 119] than in color images.

Second, there is documented implicit serial bias in visual perception [120]. Therefore, the order of images matters when presenting findings for validation. This serial bias can be a critical issue in analyzing temporal data.

Third, the representation of SRM fluorescence is often linear, for example, binning localizations per pixel, yet human visual perception is strongly nonlinear [121]. There are a wide range of methods to visualize SRM localization point clouds using a 2D image [80], although most methods are encumbered by parameters. To address this, recently parameter-free methods have been proposed [81].

Finally, visual perception is biased towards large objects, as they are more easily identified [122], yet frequency-based statistics would underrepresent these, focusing on the majority of small objects [78]. The quantitative analysis can then conflict with human visual perception. Methods adapted to stratify data, detect outliers, or interpret extreme values should accompany quantification in this case.

Recently, more powerful visualization platforms have been introduced specifically to efficiently and robustly explore high-dimensional data [123, 124, 125], mitigating some of the above issues.

### *4.9. Datasets*

Table 5 summarizes recent benchmark datasets. The inclusion criteria for the datasets to be enumerated here are that they are publicly available online and used in the validation of novel interaction analysis methods. Datasets are divided first along their 'source', that is, whether they are simulated, phantom, or real data, as described earlier. The 'label type' describes the 'detail' of the labels present in the dataset. Unsupervised refers to the absence of any discriminatory label. Weakly supervised refers to cases where object levels are absent, so one has to rely on e.g. cell or image level labels. Supervised indicates that object, localization, or pixel-level labels are available, either by annotation, simulation, or phantom data. The type or class of interaction is strongly linked to the biological use case in which the methods are validated. As is clear from Table 5, most datasets are restricted to one or two use cases or interaction types at most. In the case of multiorganelle segmentation, it is possible to have one channel with up to N types or classes of objects, between which the interaction is computed.

## 5. Novel directions in interaction analysis algorithms

Here, we provide a taxonomy of current interaction analysis methods, identifying common and diverging trends, using the earlier defined (Section 2) mathematical model to quantify scalability. A full per method breakdown is available in the appendix (Section 7).

### *5.1. Objects, density, or interaction?*

In recent interaction analysis methods, three camps emerged: discrete distance-based, density-based, and direct methods. The discrete camp first divides the data into objects by clustering, object detection, or segmentation, then the inter-object distance or overlap is computed [102, 103]. Interesting in these approaches is that UNET based CNNs are not used to segment $C$ channels [102], but rather predict $C$ segmentation masks [103] from one or two live cell channels. When crisp detection or

Table 5: Overview table of publicly available datasets for benchmarking interaction analysis methods in superresolution methods. C: Number of channels. Dim: Dimension, Label type: S(upervised), W(eakly) supervised, U(nsupervised). Data source: Re(al), Si(mulated), Ph(antom). Interaction type: (Fig. 4).

| Name | C | Dim | Modality | Data Type | Label Type | | | Interaction Type | | | | Data Source | | | URL |
|---|---|---|---|---|---|---|---|---|---|---|---|---|---|---|---|
| | | | | | S | WS | US | I | II | III | IV | Re | Ph | Si | URL |
| [126] | 2 | 3 | SMLM | P | ✓ | x | x | ✓ | x | x | x | x | x | ✓ | URL |
| [97] | 2 | 2 | SIM | V | x | ✓ | x | ✓ | ✓ | ✓ | ✓ | ✓ | x | x | URL |
| [113] | 2 | 3 | SMLM | P | x | ✓ | x | ✓ | ✓ | ✓ | ✓ | x | x | ✓ | URL |
| [39] | 2 | 3 | SMLM | P | ✓ | ✓ | x | ✓ | ✓ | x | x | ✓ | x | ✓ | URL |
| [98] | 2 | 3 | SMLM | P | ✓ | ✓ | ✓ | ✓ | ✓ | x | x | x | x | ✓ | URL |
| [40] | 2 | 3 | SMLM | P | ✓ | ✓ | ✓ | ✓ | ✓ | x | x | ✓ | ✓ | ✓ | URL |
| [109] | 2 | 3 | TREXM | V | ✓ | x | x | ✓ | ✓ | x | x | ✓ | x | x | URL |
| [102] | N | 3 | FIBSEM SR | V | ✓ | ✓ | x | ✓ | ✓ | x | x | ✓ | x | x | URL |
| [103] | 15 | 3 | Spinning disc | V | ✓ | ✓ | x | ✓ | ✓ | x | x | ✓ | x | x | URL |

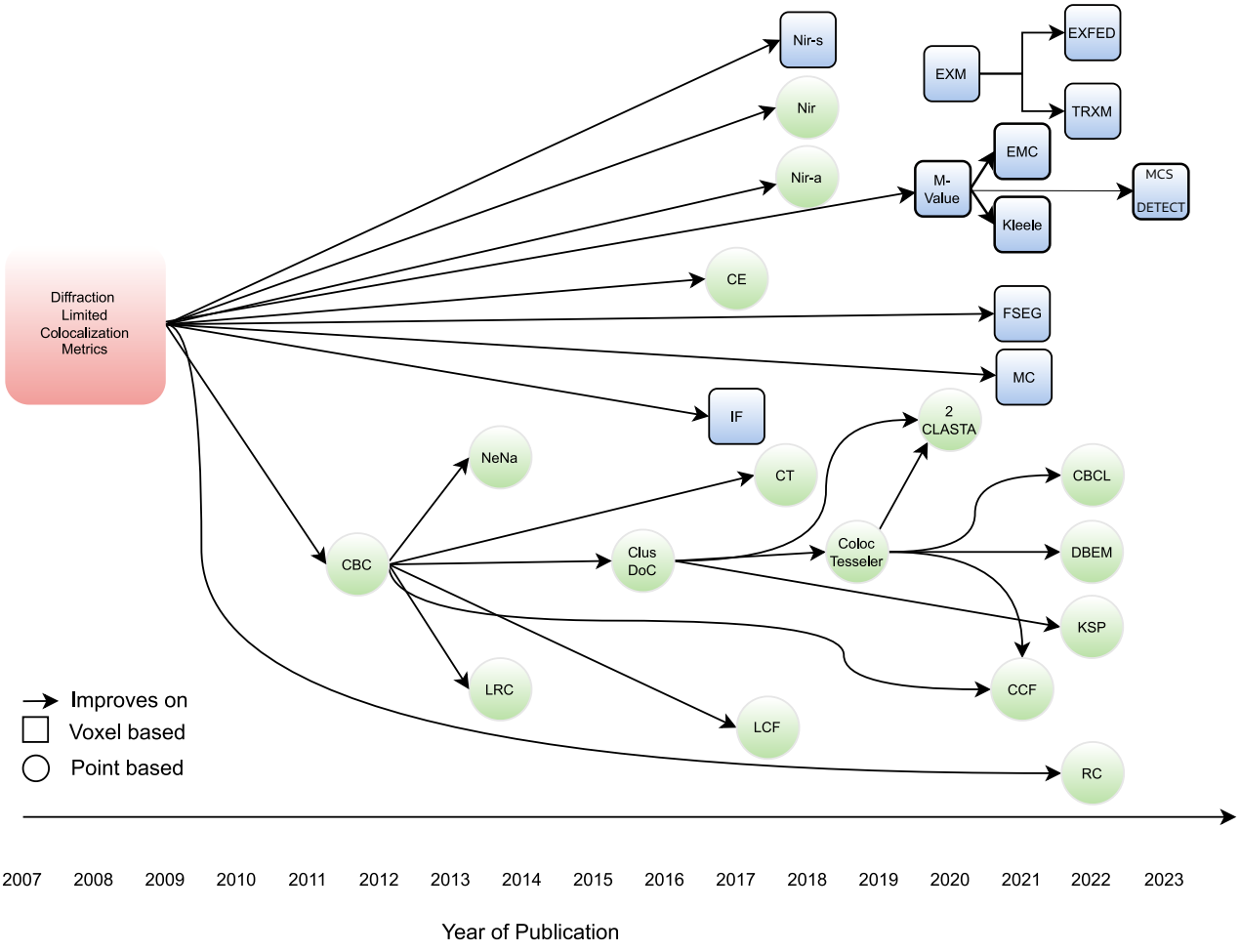


Figure 9: Genealogy of interaction analysis methods evolving over time in relation to each other. A directed arc between methods A → B indicates that B improves upon A. The resulting genealogy highlights current trends where a single method gives rise to many dependents (e.g., CBC) versus standalone contributions such as CE. The acronym of each method is cross-referenced in Table 6

Table 6: Overview table of interaction methods in superresolution microscopy. Legend: Interaction Type/Scale: I=co-occurrence, II=adjacent, III=non-zero distance/signed distance function, IV=topological. S: projection is detailed in the model section. Method names are links to the sections discussing them. When source code is available, the 'Yes' entry is a url. Symmetry denotes if $f(<a,b>) = f(<b,a>)$. In case of 'both', this occurs when a symmetric measure is built on top of asymmetric ones. In the complexity notation, $N$ is a surrogate dimension for spatio-temporal dimensions for voxel based data, or density for point clouds. $R$ is a parameter-dependent complexity variable, $M$ refers to localizations per frame, $M << N$.

| Name | Ref | Year | CR | Improves On | (In)Direct | $C$ | $D$ | Modality | Data Type | Computational Complexity | Interaction Type\|Scale | $\theta$ | Symmetry | Source Code | Biology Use Case |
|---|---|---|---|---|---|---|---|---|---|---|---|---|---|---|---|
| M-Value | [127] | 2020 | ↓ | Manders | Indirect | 2 | 3 | SIM/STED | V | O(N) | I-II | 3 | Yes | No | Mito<br>Lysosome |
| CBC | [93] | 2012 | ↓ | Manders | Direct | 2 | 3 | SMLM | P | O(R N log N) | I-II | 3 | Both | No | Actin in Hela<br>Microtubulin |
| ClusDoC | [66] | 2016 | ↓ | CBC | Indirect | 2 | 3 | SMLM | P | O(R N log N) | I-II | 7 | Both | Yes | Focal Adhesion<br>T-Cell receptor |
| CCF | [126] | 2021 | = | CBC<br>CT | Indirect | 2 | 3 | SMLM | P | O(N log N) | I | 2 | Yes | Yes | ULK1<br>ATG13 |
| ColocTesseler | [74] | 2019 | ↓ | ClusDoC | Indirect | 2 | 3 | SMLM | P | O(N log N + $N^{\frac{d+1}{2}}$) | I+II | 1 | Yes | Yes | Tubulin<br>Synapses |
| Kleele | [97] | 2021 | = | M-Value | Indirect | 2 | 3 | SIM | V | O(N) | I+II+III+IV | 2+ | Yes | Yes | Mitochondria<br>Fission |
| 2-CLASTA | [113] | 2020 | = | CTesseler<br>ClusDoc | Direct | 2 | 3 | SMLM | P | O($RN \log N$) | I+II+III+IV | *0* | No | Yes | K-mers<br>In silico |
| CBCL | [39] | 2022 | ↓ | CTesseler<br>ClusDoc | Direct | 2 | 3 | SMLM | P | O($RN \log N$) | I+II | *0* | No | Yes | Tubulin<br>Synaps |
| DBEM | [98] | 2022 | = | CTesseler<br>ClusDoc<br>GF | Indirect | 2 | 3 | SMLM | P | O(N log N + $N^{\frac{d+1}{2}}$) | I+II | *0* | No | Yes | Vesicle<br>Synaps |
| LCF | [40] | 2018 | = | Manders<br>CBC | Indirect | 2 | 3 | SMLM | P | O(R N log N) | I+II | 3+ | Both | Yes | DNA Repair |
| IF | [128] | 2017 | = | Manders<br>Pearson | Indirect | 2 | 3 | SMLM | V | O(R N) | I | 1 | No | Yes | DNA Repair |
| Nir-$\alpha$ | [67] | 2018 | ↓ | Manders<br>Pearson | Indirect | 2 | 3 | SMLM | P | O(N log N + $N^{\frac{d+1}{2}}$) | I-II | 1 | No | Yes | Chromosome |
| Nir-fuzzy | [67] | 2018 | ↑ | Manders<br>Pearson | Indirect | 2 | 2 | SMLM | P | O($N^2$) | I-II-III | 1 | No | Yes | Chromosome |
| Nir-segmented | [67] | 2018 | ↓ | Manders<br>Pearson | Indirect | 2 | 2 | SMLM | V | O($N$) | I-II | 1 | No | Yes | Chromosome |
| CE | [95] | 2017 | ↓ | Manders<br>Pearson | Indirect | 2 | 2 | PALM | P/V | O($RN \log N$) | I-II-III-IV | 1 | No | No | Chromatin domains |
| NeNa | [44] | 2014 | ↓ | Manders<br>Pearson | Indirect | 2 | 3 | SMLM | P | O($N \log M$) | I-II | *0* | No | Yes | Microtubule |
| EXM | [129] | 2020 | = | M-Value | Indirect | 4 | 3 | EXM<br>STED/SIM | V | O($N$) | I-II | *0* | Yes | No | Mitochondria Cristae |
| TRX | [109] | 2022 | ↓ | EXM | Indirect | 2 | 3 | TRX/EXM<br>STED/SIM | V | O($N$) | I-II | *0* | No | No | Synapse<br>Microtubule<br>Nanopore |
| ExFED | [108] | 2022 | = | TRX | Indirect | 2 | 3 | ExFED | V | O($N$) | I-II | *0* | No | No | Hela Microtubule |
| CT | [94] | 2018 | ↓ | ClusDoC<br>CBC | Indirect | 2 | 3 | SMLM | P | O($N^2$) - O($N \log N$) | I-II | *3* | Yes | Yes | Chromatin domains |
| LRC | [13] | 2014 | ↑ | CBC | Indirect | 2+ | 2-3 | SMLM | P | O($N \log N$) | I-II | 1 | No | No | Chromatin T-cell synapse |
| KSP | [100] | 2022 | ↓ | ClusDoC | Indirect | 2 | 3 | SMLM | P/V | O($N$) | I-II | 1 | No | Yes | T-cell synapse |
| RC | [35] | 2022 | ↓ | N/A | Direct | 2+ | 3 | SMLM | P/V | O(1) - O($RN \log N$) | I-II | 2 | No | No | N/A |
| FSEG | [102] | 2021 | ↓ | Manders | Indirect | 2+ | 3 | FIBSEM | V | ? | I-II | $\theta_{CNN}$ + 4+ | No | Yes | Whole Cell |
| MC | [103] | 2021 | ↑ | N/A | Indirect | 15 | 3 | SRM | V | ? | I-IV | $\theta_{CNN}$ | No | Yes | Whole Cell, HeLa, Cos7 |
| EMC | [110] | 2021 | = | M-Value | Direct | 2 | 3 | 3-4D STED | V | O(N) | I-II | *0* | No | No | Neuronal MAM |
| MCS-DETECT | [3] | 2023 | = | M-Value | Direct | 2 | 3 | 3-4D STED | V | $O(N((2*w+1)^3)\log(2*w+1)^3)$ | I-III | 4 | No | Yes | MAM/MERC |

segmentation is non-trivial, an alternative direction uses density estimation, for example, computing the correlation between estimated density functions. A well-known method for estimating density under isotropic assumptions is the Ripley family of functions [66, 13]. Another indirect and popular representation of density is tessellation, which has become a popular intermediate platform for building interaction analysis methods on [98, 74]. In voxel space, supervised segmentation can be imprecise and overfit to training data [103]; instead, the intensity of both channels can be analyzed using FWHM-based [110, 127, 97] or correlation-based [93] methods. A related approach uses the correlation of the second derivative of the intensity [3] to reduce sensitivity to fluctuation in intensity per channel.

Finally, direct methods are those that omit all intermediate stages and output a single interaction score. Recent examples are Baragilly's KS-test [100] and Arnold et al.'s 2-CLASTA [113].

### 5.2. *Heterogeneity, calibration through model fitting, and specialization.*

A second stratification in novel methods is the specialization toward specific use cases, which leads to increased diversification of methods. In Table 6 the use case and interaction scale is listed for each method, allowing the reader to view the stratification of methods per category, with each detailed in the appendix Section 7. For example, labeling the same structure, such as microtubules, with two different markers is a frequent use case for validating or calibrating Type I interaction methods. Other frequent use cases are Mitochondria-ER Contact (MERC)s and studies related to the neural synapse (Type II-III).

Validation in SRM interaction is non-trivial and made more complex by methods with large parameter spaces. The need for adaptive or self-tuning methods is clear in the emergence of parameter-free methods [39, 98, 110]. However, this is not always feasible; for example, deep learning-based approaches invariably come with large parameter spaces [102, 103] in their training stage. The presence of parameters is not necessarily problematic, but their impact on consistent (Section 4.7) performance and understanding how to configure them is. Parameter consistency studies are typical for most interaction analysis methods, with particular focus on consistency in the presence of stronger confounding factors [130]. However, what is equally clear is that even parameter-free methods will in the end be 'calibrated'. A method with a range of [0-1], designed to capture co-occurrence, is expected to output 1 when applied to a structure labelled by two distinct labels. In practice, such a maximum value may not occur due to SNR, imaging, labeling, and so on. Interaction analysis methods are tested and calibrated on biological data; in the above scenario, an example maximum practical value of 0.85 would then be equated to an interpretation scale. For example, the mitochondria lysosome interaction value (M-Value) [127] splits its range into two cases based on biological ground truth in postprocessing. An example of this in correlation-based methods is the interaction factor (IF) [128] of Bermudez et al.[128].

### 5.3. *Scalability necessitates adaptive algorithms*

SRM data are inherently orders of magnitude larger than confocal imaging of the same specimen, which requires that novel methods are designed to be scalable. To this end, our taxonomy explicitly computes the computational complexity, which describes a function that models the best, average, or worst-case running time as a function of the input size. A prime example of scalability driving development is cross-correlation filtering (CCF) [126] where cross-correlation is used to filter cross channel distances. Preprocessing, such as 'particle averaging' or denoising, can be used to reduce running time. For example, the often used Density-Based Spatial Clustering of Applications with Noise (DBSCAN) [65] algorithm is designed to work with noisy data, yet Pageon et al.[66] explicitly 'denoise' data before clustering with DBSCAN, simply due to the prohibitive running time on large point cloud datasets.

Approximating the interaction by observing the pairwise distance in SMLM is a common approach [93, 39, 126]. However, a naive all-to-all computation has a quadratic runtime and memory usage. To make interaction methods scalable, we observe a three-pronged approach to this problem. First, using optimized data structures such as a K-Dimensional Tree (KD-Tree) can dramatically speed up distance computations, as demonstrated by Mancebo et al.[126]. Second, some leverage the observation that the all-to-all distance matrix can be represented with a minimum loss of information by 'geometric spanners' (g-spanner) [131]. A g-spanner retains reduced connectivity between points, yet guarantees that the distance between any two points is approximated up to a constant factor by the connected path distance between the two. A frequently used example of this are tessellations [74] or the equivalent triangulation. K-nearest neighbour representations can be g-spanners, though the selection of $k$ needs to be done carefully. Third, thresholding the long tail of the distance distribution is an alternative method that can reduce unnecessary distance computations [126]. In the worst case, a fixed distance or density threshold is established.

Scalability goes hand in hand with efficient data storage formats, with rapidly increasing volumetric and pointillist data, illustrated by the novel scalable formats introduced [30, 87, 132].

### 5.4. *Distance: Asymmetry can be useful*

Pairwise proximity between objects in the discrete paradigm is frequently measured by either the nearest neighbour or the K-nearest neighbour distance. This is a directed measure; if object A in channel one is nearest to object B in channel two, the opposite is not necessarily true. Although distance-based methods are typically asymmetric [13, 67, 39, 98, 40], they can be made symmetric by aggregation of both directed distances, as in the commonly used Chamfer distance. As discussed in the model section on 'order' of interaction (Section 2.3), this can complicate application to more than two channels, rapidly escalating to combinatoric complexity. Directed distance is still of use as it can isolate the functional relationship between objects of interest. For example, objects in channel A may interact with many other objects, but if objects in channel B are specific in their interaction, then a directed asymmetric distance from B to A is more precise than a symmetric distance.

### 5.5. Interaction beyond pairwise: closing the multichannel gap

With functional pathways invariably involving more than two proteins or organelles, interaction analysis should move beyond pairwise analysis. Although a straightforward extension of existing methods is not always feasible, alternative approaches can close this gap. For example, Zhanghao et al.[103] use DL-based synthesis where, given 2 channels, up to 15 distinct 'channels', or semantic segmentation inputs interaction predictions are made. This method is particularly notable because each target is specific to one organelle and trained with weakly supervised data, ensuring high specificity and avoiding the organelle-specific bias present in other methods (e.g., [102]).

A critical step in closing the multichannel gap are 'direct' methods. Direct methods are those that are 'end-to-end', they take in the data and output a single interaction output [113, 128]. In contrast, 'indirect' methods [3, 95, 74] are typical pipelines composed, frequently out of necessity, of modular steps tackling individual problems before generating the interaction output. In Table 6 we categorize each reviewed method (Section 5) along this criterion. While indirect methods can be more flexible, direct methods can be computationally more efficient and less encumbered by parameters, and thus better suited to multichannel analysis beyond pairwise. The recent introduction of highly multiplexed modalities [8] underlines the urgency to close the 'multichannel gap'.

### 5.6. Interaction beyond distance: the randomized approach

As discussed and illustrated earlier (Fig. 8-A), distance is an indirect observation of, but not equal to interaction. Compromising factors (Fig. 7, Section 3) can easily skew the random probability of two objects occurring at a given distance [73]. While causal-based methods for recovering interaction from distance and state changes are yet to be published, the next best thing are randomization experiments or closed form equations modeling this effect. Such randomization experiments try to de-correlate interaction distance from expected distance (Section 3.8, Eq. (16)). Bermudez et al. [128] use randomization of objects to define a self-calibrating direct IF (Section 7.13). In contrast to empirical randomization, which can be computationally intensive and requires careful choises in distributions, Åberg et al.[35] derive closed-form equations for the probability of proximity of objects in the cell to calibrate interaction analysis results.

### 5.7. The odd ducks in the group: diverging and emerging trends

SMLM reconstruction algorithms are rarely used for semantic tasks. However, they frequently address similar conceptual challenges that semantic methods would address. Consequently, examining trends in this domain enables us to pinpoint intriguing avenues for future research. For example, point-cloud registration implicitly or explicitly involves quantifying the disparity between two point clouds, thus potentially negating interaction mediated by distance. It should be noted here that there is a recent move toward reconstructing structures with less predictable shape priors [61] as well as the explicit incorporation of precision and uncertainty [44, 39]. Indeed, although the uncertainty in localization is typically observed in SRM data, only a limited number of techniques explicitly leverage it to enhance the precision of interaction reconstruction [39, 40, 95].

## 6. Discussion

In this section we conclude the review by shedding light on open problems in interaction analysis.

### 6.1. The multichannel gap: challenges in interaction beyond two channels

The combination of parameter-encumbered methods and the high 'order'(Section 2.3) of many interaction methods prohibits extending many methods beyond two channels, yet this is clearly where the future potential for discovery lies. Some symmetric methods, such as correlation-based methods [3, 13, 39, 93], can be extended without major changes, as multivariate correlation is well defined and actively developed [133]. Alternatively, generative [134] or multiclass segmentation models [103, 102] can avoid the acquisition of more than one or two channels altogether. However, currently, this is limited to organelle-based studies. For example, predicting the nanodomains of the dozen or so proteins on the mitochondrial membrane involved in MERC interaction is not yet feasible but of great interest. In part this is due to the absence of validation at the protein level, whereas knowledge on appearance and geometry of organelles is far better documented and can be validated in other modalities. Here we see again the tension between discovery and validation, to show a method can discover new knowledge, somehow the novel discovery needs to be validated. However, perfect validation implies that there is no need for a new tool to re-discover what is already known.

Krueger et al.[135] demonstrated that joint supervised and unsupervised learning can bridge the multichannel gap in high-throughput single cell imaging, illustrating an important point: you do not need to restrict a method only to supervised, weakly supervised, or unsupervised paradigms; instead, combining these in modular stages can be quite powerful. However, such hybridization and modularity can also make multi-channel analysis more complex and prohibit scaling beyond specific use cases. Randomization approaches [73] are very valuable but can be prohibitively expensive. Under limited assumptions, closed-form equations [35] can be derived that eliminate the computational cost altogether.

Closing the multichannel gap will require scalable algorithms. One approach to improve scalability is to decompose algorithms into modular components that can be optimized, replaced with versions with lower algorithmic complexity, and distributed to run on dedicated cluster computing hardware. Even though interaction analysis algorithms often utilize common computational building blocks, such as nearest-neighbour lookup, frequency counting, peak finding, we observed that these implementations typically do not leverage optimized APIs

to accelerate and delegate these common tasks. A worrying trend is to favor the reuse or re-implementation [66] of deprecated versions algorithms to solve these subproblems rather than rely on markedly improved art from high performance computing [136, 137, 138]. Such decomposition and modularization, in addition to accelerating existing methods, would make their integration into frameworks that can run on clusters easier [139, 140, 141, 142, 143].

### 6.2. *Specialization and absence of reference datasets limits reproducibility*

There is a shortage of open, diverse, and multiscale datasets for interaction analysis, in part due to the specialization of methods onto specific interaction scales and use cases. Consequently, a typical paper on interaction analysis methods will feature new data, including newly simulated data as well. A set of public, diverse, and multichannel datasets as well as re-using established simulators can prevent potential overfitting and conserve resources. The logistical challenge of making these datasets available is remediated by the recent rise of dataset sharing platforms such as Zenodo, IEEE DataPort, and the Open Science Framework.

### 6.3. *Novel directions to jointly capture state and distance*

While a minority of methods start from a mathematical model of interaction, often this is limited to modelling the joint emission properties (PSF, SNR, etc.) rather than the full causal model of interaction. However, we have shown that such a decomposition (Section 2) is perfectly feasible by providing it for both pointillist and voxelized methods.

The wide spectrum of compromising factors enumerated here is in practice frequently under-explored during the development and introduction of novel interaction analysis methods. For example, a majority of methods exclude state change in interaction and focus solely on distance. Defining interaction by distance alone is demonstrably insufficient [73, 35]. This is in part because capturing state change in pointillist data is non-trivial, as segmentation and clustering for this data are still open problems [25]. Novel quasi-interpretable mathematical models, such as persistent homology, can offer an alternative by providing semi-interpretable quantification of pointillist data [144]. A different approach is offered by using self-supervised learning (SSL) approaches developed for microscopy [145, 146], with the added advantage of reducing the annotation burden. To tackle the sparsity and complexity of validation, an interesting direction is using 'phantom' intervention as validation in optogenetics [147]. Here, genotypes are modified to be light-activated, resulting in live-cell observable state and location changes. In line with our observations, Vasudevan et al. [148] argue that current DL paradigms lack an explicit or implicit causal aspect to be useful in fields such as microscopy. They argue that sparse models can be capable of processing terabyte-scale datasets without requiring equally large neural network models.

### 6.4. *Conclusion*

In this paper, we gave an in-depth overview of novel interaction methods in SRM. We discuss the factors that can compromise interaction analysis and discussed strategies in validation with sparse ground truth. We illustrated the absence of a common mathematical model and then showed that such a causal-based model can be projected onto the state-of-the-art. We enumerated selected works from the state of the art in interaction analysis, reviewing each in detail and providing both open problems, future directions, and emerging trends. We concluded by identifying the 'multichannel gap' as the main direction where research will focus in the next few years and what open problems need to be resolved to address this gap.

### 6.5. *Acknowledgements*

We thank Timothy Wong for his insightful comments that helped improve this work. Discussions in the Hamarneh and Nabi labs further helped improve the messages and insights bundled in this work. This study was supported by grants from the Canadian Institutes of Health Research (CIHR: AWD-022443, PJT-148698) and from the Natural Sciences and Engineering Research Council of Canada (NSERC: RGPIN-2019-05179, RGPIN-2020-06752).

### 6.6. *Declaration of Interests*

The authors declare no competing interests.

## 7. Appendix

Here, we briefly review each method discussed in the paper along the dimensions in Table. 6 and the mathematical framework introduced earlier. For each method, the complexity and the mathematical mapping is derived.

### 7.1. Correlating Ripley functions: LRC

Rossy et al [13] introduce Getis and Franklin (GF) [109]-based local point pattern analysis to quantify colocalization in SMLM, with a calibrated search radius $r$, as a response to coordinate based colocalization (CBC) [93]'s automatic coefficient. The main idea is to contrast or correlate Ripley's $L(r)$ and $L_{cross}(r)$ functions, to describe relative ratios of adjacent or overlapping densities (I-II). For localizations $i, j$ and the real value threshold $r \in \mathbb{R}^+$, let $l, k$ be indices of channels:

$$\delta_{r,k,l}(i_k, j_l) = \begin{cases} 1 & \|i_k - j_l\| < r \\ 0 & \text{otherwise} \end{cases} \tag{23}$$

$$L(r,l,k) = \sqrt{A \sum_{i=1}^{N} \frac{\delta_{r,l,k}(i,j)}{N\pi}}. \tag{24}$$

where $A$ is the area of analysis, and $N$ the total number of points in $A$. Edge effects are compensated by clearing a buffer at the edge of radius $r$. $L_{cross}$ then simply is $L(r, 1, 2)$. This is an indirect measure, asymmetric, and sensitive to effects such as multiple blinking, while it also does not account for uncertainty and random distance effects. Source code, nor data, are available. Complexity is not listed, but can be computed in $O(N \log N)$, or faster when using a geometric spanner[131] such as Delauany or tesselation. The mapping is given by:

$$f_{\theta=r,SR_{\uparrow}} :< P_1^2, P_2^2 > \rightarrow < P_{[0,1]}^2 > . \tag{25}$$

It is in principle an expansion, because for each point the local density $L(r)$ is computed, but also the cross channel density, before they are compressed.

### 7.2. M-value: FWHM based analysis

Chen et al.[127] introduce the M-Value, a ratio between 0 and 1 that uses the FWHM of merged channels to quantify interaction between mitochondria and lysosomes in SIM. For two channels $(V_1, V_2)$, the M-Value is defined as:

$$M = \frac{Y}{\min(FWHM(V_1), FWHM(V_2))}, \tag{26}$$

where Y is the merging distance. The mathematical model is:

$$f_{\theta=window,SR_{\downarrow}} :< V_1^2, V_2^2 > \rightarrow < V_{mvalue,[0,1]}^2 > . \tag{27}$$

The M-Value is a windowed or ROI based mapping (Eqn. 26), and is claimed to be more robust than pixel based metrics, such as Pearson or Manders, because those do not take into account the intensity profile, and can suffer adversely from low SNR. The M-Value is similar to Manders at the FWHM level, rather than pixel level, or comparable to intersection of FWHM over union metrics. Such an approach is sensitive to bleedthrough. For interpretation and validation, Chen et al.[127] derive empirical observed threshold values for this reporter in function of different interaction between mitochondria and lysosomes, and link those to semantic differences. Source code is not available. Estimating FWHMis a linear operation, so overall complexity is linear in input: $O(N)$. While the FWHM (Eqn. 18) can be a robust reporter, using this value on the intersection of two channels is sensitive to intensity fluctuations in either channel. As the reader will appreciate from the equation (Eqn. 18), it is well suited to smooth symmetric intensity profiles. Asymmetric intensity profiles, for example due to variable expression or labelling, could quickly compromise this method. Its sensitivity to asymmetric intensity profile notwithstanding, the M-Value is symmetric.

### 7.3. MCS-DETECT: Segmentation free reconstruction of ER-Mitochondria contacts (MERCS)

Improving on FWHM-based methods the Membrane Contact Site Detection (MCS-DETECT) [3] algorithm was introduced for 3D STED detection and reconstruction of MERCs without requiring segmentation. By building a joint probability per voxel using several windowed differentials the method is able to be both stable and robust. Complexity is $O(N(2 * w + 1)^3 \log(2 * w + 1)^3)$ in 3D for a window size of $w$. Scalability is ensured by multithreaded execution. MCS-DETECT is symmetric, and has 4 parameters that determine the window size, the confidence levels, and the background filtering. The mathematical model is:

$$f_{\theta=window,SR_{\downarrow}} :< V_1^3, V_2^3 > \rightarrow < V_{mcsdetect,[0,1]}^3, V_{confidence,[0,1]}^3 > . \tag{28}$$

Validation is done by contrasting 3 distinct cell lines, in 3D, and 5 conditions in total, and correctly reproducing statistics previously only observed in 2D EM ROIs. A key advantage is the bleedthrough filter that removes artifacts in both channels adaptively, avoiding false positives.

### 7.4. Mitochondria Fission signatures

Kleele et al.[97] investigate mitochondrial fission dynamics in structured illumination microscopy, a critical mechanism in cellular health where the sub-organelle mitochondria in the cell divide in response to damage, oxidative stress, or energy requirements. This use case is quite interesting because the interaction occurs between objects of the same channel (mitochondria), and is probabilistic because it transitions from co-occurrence (I), to adjacency (II), and to proximity (III). In addition, topological analysis (IV) then allows them to quantify the location of fission with respect to the 'whole' mitochondria to determine 'healthy' versus 'pathological' fission dynamics. The method itself is an 'indirect' pipeline of segmentation, followed by identifying the 'constriction' site by a biological marker. The FWHM of the marker was thresholded as a constriction classification method. Mitochondrial fission involves the ER, intensity filtering of 2x threshold was used to infer a

contact at constriction sites. Precision of the system does not allow a more precise detection. The mapping then is

$$f_{\theta=T,N,SR_{=}} :< V_1^3, V_2^3 >\rightarrow< V_{kleele,\{0,1\}}^3 >, \tag{29}$$

while this is clearly an indirect, symmetric measure, with several thresholding parameters. The mapping remains 'onto'. Computational complexity is, with the exception of the segmentation training, O(N).

### 7.5. Coordinate based colocalization (CBC): Spearman correlation of density gradient

CBC [93], briefly, computes the Spearman correlation of density coefficients, has a range of [-1,1] where 0 indicates random occurrence or no semantic colocalization, -1 indicates repellence, and 1 perfect colocalization.

$$D_{Ai,A}(r) = \frac{N_{A_i,A}(r)}{\pi r^2} \times \frac{\pi R_{max}^2}{N_{A_i,A} R_{max}}, \tag{30}$$

where r is a radius, $R_{max}$ is the maximum distance. The term $N_{A_i,A}(r)$ is the density of points in $A$ in a radius $r$ w.r.t. $A_i$. Next a Spearman coefficient $SR_{A_i}$ is computed for the range of r using $D$ contrast to A and B channels. Finally, the CBC value is

$$C_{A_i} = SR_{A_i} \exp -\frac{E_{A_i,B}}{R_{max}}. \tag{31}$$

The mathematical model is then:

$$f_{\theta=R_{max},R,SR_{\downarrow}} :< P_1^3, P_2^3 >\rightarrow< V_{cbc,[-1,1]}^2 > . \tag{32}$$

While not given, a Spearman computation allows the computation of significance value, so in principle a paired 'c' function could be implemented. In plain language: for each point a corresponding value is computed, in 3D. Metadata such as precision of acquisition is not used. Computational complexity of CBC is not given, but can be estimated by the sub-problems it tackles: counting nearest neighbours and Spearman correlation. With a KD-Tree implementation, frequently optimal for 3D point cloud operations, this is $O(N \log N)$ It can be optimized by e.g. caching to exploit localized retrievals, and restricting the maximum distance, but the essential complexity is not changed by those. The advantages of CBC is that it produces a per-point value, and scales with the distribution of points. While $R_{max}$ can be a parameter, it does not need to be, so parameter space is small and the method is adaptive. A somewhat hidden parameter is step size, in principle CBC is continuous over $r$, but in practice it is not. Step size will thus be a user defined value that can affect results. CBC is, however, restricted to either adjacency or colocalization. Two points can have a CBC of -1 and be double the distance away from the colocalization points. CBC values are often discretized, because there is no direct mapping of $C$ to 'yes there is colocalization'. Ideally, using a significance score would make this selection more robust, a $C$ value can be identical for 1 sparse point near 100 points, and 1 sparse point near 1000 points. Finally, nearest neighbour algorithms are sensitive to noise and variable precision, as well as the multiple blinking problem. The individual terms of CBC are not symmetric, but the combined contrasted correlation is.

### 7.6. Clus-DoC: CBC meets DBSCAN

CBC (Section 7.5) is sensitive to noise and requires to be clustered to resolve points to localizations, and more importantly, points to semantic (protein) structures. clustering based colocalization (Clus-DoC) [66] combines DBSCAN as a clustering method with CBC to colocalize protein localizations in SMLM. A variant of the Ripley K function is used to denoise, for a distribution of m points p and radius r:

$$K(r) = \frac{1}{\lambda m} \sum_{i=1}^{m} \sum_{i \neq j}^{m} I\|p_i - p_j\| < re_{ij}(r). \tag{33}$$

Here, $\lambda = \frac{m}{V_{ROI}}$, the density of points over the volume. $e$ is an edge correction, calibrated for edge-induced spatial effects. The $L(r)$ function is then defined as:

$$L(r) - r = \sqrt{K(r)/\pi} - r. \tag{34}$$

Noise filtering in Clus-DoC is defined as points where $L(r) - r$is below the value of randomly placed data, where $r = 50$ nm. Naturally, this leaves open the choice of what is considered 'random' data, and how well that correlates with noise. Subsequently DBSCAN clusters localizations. The choice for DBSCAN, and not one of its modern variants [136, 137, 138], is odd and not justified, especially because DBSCAN is quite sensitive to its 2 key parameters, if one uses Euclidean distance as a default distance function. Data was not released to reproduce. Complexity is not mentioned, but again we can reconstruct this from the actual computing science problems being solved. We established CBC has a complexity of $O(RN \log N)$, for R steps. Ripley's K function uses the same functionality of nearest neighbour lookup, and so can be computed in $O(RN \log N)$ for R steps. Complexity of DBSCAN is $O(N \log N)$. The denoising step, using Ripley's K, is odd because DBSCAN was originally proposed to work in the presence noisy datapoints, and is more likely chosen to reduce the runtime complexity. For similar reasons, an ROI based approach is suggested to configure denoising parameters. The mapping is:

$$f_{\theta=R_{max},R,D1,D2,e,SR_{\downarrow}} :< P_1^3, P_2^3 >\rightarrow< P_{clusdoc,[-1,1]}^2 > . \tag{35}$$

Given that it is using CBC, it is a symmetric measure.

### 7.7. Efficient Cross-Correlation Filtering (CCF): speeding up NN queries by thresholding

CCF proposes cross-correlation filtering to quantify colocalization. The key contribution is to use a KD-Tree representation to store pair wise distances, and to threshold distances based on the distribution, typically long-tail, of those distances. No automation is provided to do the thresholding. Improved memory usage is reported compared to Clus-DoC and CLT [74]. Computation complexity is the same: O(N log N), however, the advantages in the comparison are due to Clus-DoC using a DBSCAN variant that is not optimized. Colocalization is determined by a distance based threshold. However, this approach

would lend itself to future improvements by becoming adaptive, that is, finding the aforementioned thresholds automatically based on the long-tail shape of the distribution. CCF is symmetric.

$$f_{\theta=R_{max},R,D1,D2,e,SR_{=}} :< P_1^3, P_2^3 >\rightarrow< P^3_{ccf,[-1,1]} > . \quad (36)$$

### 7.8. Coloc-Tesseler: pairwise classifying tesselations

CLT is an extension of the frequently used Voronoi-tesselation method to represent the density of the point cloud by areas of Voronoi cells. Voronoi diagrams of a set of points are the dual of a Delaunay triangulation, construction of which for points in d-dimensions is $O(N \log N + N^{\frac{d+1}{2}})$. The preference of Voronoi diagrams over its dual stems from the ease of filtering out 'edge-effects'. Both Voronoi and Delaunay triangulations of a set of points have the property that they are 'geometric spanners', that is, seen as a graph they approximate the complete graph within a fixed factor. The complete graph, with an edge between any two pairs of points, encoded the complete distance distribution. However, for N points this requires $O(N^2)$ space, and is often not needed for downstream tasks, an approximation is sufficient.

A KD-Tree or ball-tree is one efficient representation to quickly and efficiently lookup distances between points by storing adjacent points together in a tree-like datastructure. In contrast, in a triangulation, to lookup the distance between any two points $u, v$, it is sufficient to follow the shortest path $\langle u, v\rangle$ in the triangulation. By the property of being a geometric spanner [131], the length of this path is then within a constant factor $k > 0$ of the Euclidean distance between u and v, or the edge $\langle u, v\rangle_C$ in a complete graph: $\|\langle u, v\rangle_C\| < k\|\langle u, v\rangle\|$. This sidebar is of interest because a significant section of clustering and analysis methods in SMLM work on Delaunay or Voronoi representations. CLT constructs a tessellation for each channel. Then, it classifies the joint tessellation in first 3 subsets, based on a density threshold $T$: $C^A, C^B, C^{\overline{AB}}$: areas dense in A, B, and neither. The two dense classes are then subdivided in paired dense and dense-sparse. The resulting representations are then used as a basis for Manders, using the area of the cells instead of pixels, and Spearman correlation of density. The complexity is O(N log N + N log N + $N^{\frac{d+1}{2}}$) when using optimized data structures. The critical parameter is $T$, which defines 'low density' versus 'high density'.

$$f_{\theta=T,SR_{\downarrow}} :< P_1^3, P_2^3 >\rightarrow< P^3_{coloct,[-1,1]} > . \quad (37)$$

CLT is listed here as a compression because the interim colocalization representation of classified areas is a compression, but on top of this are then multiple metrics computed, that have different signatures.

### 7.9. Verifying molecular clusters by 2-color localization microscopy and significance testing - 2-CLASTA

Arnold et al [113] introduce 2-channel colocalization by statistical analysis (2CLASTA) [113], a statistical method to determine the significance of colocalization (I-II) in SMLM. It is designed to be parameter free, and does not require clustering or denoising. As such, this is a 'direct' method. 2CLASTA works by testing the hypothesis that the (k) nearest neighbour distance across channels is with high significance not originating from a random distance distribution. It does this by inducing a randomized distance distribution by shifting points, and comparing the distributions. While in principle parameter free, k is varied, and is influenced by the point distribution. The maximum distance $R_{max}$ is set by the actual cell data. It is not significantly affected by registration or multiple blinking, and showed a capability of discriminating between k-mers. The mapping then is given by:

$$f_{2CLASTA,\theta=\emptyset,SR_{\downarrow}} :< P_1^3, P_2^3 >\rightarrow< P^3_{2clasta,[0,1]} > . \quad (38)$$

Complexity is O($RN \log N$) for fast distance lookup, with R randomized samples. This clearly is not a symmetric metric, though it can be in practice. It is noted that this method is sensitive to cell shape effects, for example.

### 7.10. Coordinate Based CoLocalization: fuzzy adaptive nearest neighbour density

Willems et al.[39] introduce localization of coordinate based colocalization (CBCL) [39], a method for interaction types I and II, that takes into account the uncertainty in localization. They estimate the local density $LD$, per localization, to offset topological and randomization effects. They estimate the distance $d$, within which the density $LD$ is computed, by $d = \sqrt{MNND^2 + \epsilon^2}$ where $MNND$ is the mean nearest neighbour distance, and $\epsilon$ the localization precision. A directional colocalization coefficient can then be computed, for the i'th point in channel A:

$$CI_i^A = \frac{N^B_{A_i} d_B}{\overline{LD_B}} \quad (39)$$

and vice versa for B. This is clearly an asymmetric measure, suited for I-II scale of interaction, as it quantifies equality of local density. It is sensitive to multiple blinking and differing SNR. The mapping is

$$f_{cbcl,\theta=\emptyset,SR_{\downarrow}} :< P_1^3, P_2^3 >\rightarrow< P^3_{cbcl,1\rightarrow2}, P^3_{cbcl,2\rightarrow1} > . \quad (40)$$

CBCL is unique in that it is one of few methods that compensates for the localization error in estimating point cloud density.

### 7.11. Density-based enrichment measure: frequency discretized over tesselation

Ejdrup et al [98] introduce density based enrichment measure (DBEM) [20] as a direct improvement on Clus-DoC, CBC, CLT, and GF. While they claim e.g. Clus-DoC cannot work on 3D, this is not an algorithmic, but implementation restriction. Their key contribution is that they propose a parameter free, point-wise metric. This directional method, for two point clouds $P_A^3, P_B^3$, works by creating a tessellation for B $T_B(P_B^3)$, then counting the frequency, per tessellation cell, of points of $P_A$ in $T_B$. A 'relative enrichment' value is then computed, a ratio of this localized frequency with respect to the expected value of localizations per area overall. This is an asymmetric measure, with complexity dominated by the tessellation and

lookup of localizations in the cells, which can be done efficiently with a KD-Tree. Validation is done on in silico vesicle simulations, and neuron synapse data. The interaction scale is I-II. Weaknesses are anisotropy and reliance on the expectation value, which can be induced by e.g. cell, as well as sensitivity on the multiple blinking problem. The mapping is given by:

$$f_{DBEM,SR_{=}} :< P_1^3, P_2^3 >\rightarrow< P_3^3 > . \tag{41}$$

No confidence value is presented. In long tail data it is trivial to skew an expected value, so an improvement could be used the sampled mean, or more robust statistics.

### 7.12. Localization Correlation Framework (LCF) - formal derivations enables leveraging uncertainty

Schnitzbauer et al.propose the localization correlation framework (LCF) [40] for both spatial and temporal analysis using correlation of point data. Key advantages of over approaches such as CBC is that localization uncertainty can be incorporated, and the derivation is shown to be onto the pixel wise correlation. The ability to use the framework for temporal analysis is very valuable as well. The core idea is to extend the cross correlation function, for 2 images $V_A^2, V_B^2$ to a coordinate based function that will end up encoding the displacement vector $P_A^3 = T_{AB}(P_B^3)$, indexed at spatial coordinates. For shifts $\alpha, \beta, \gamma$, and point cloud data $P_A^2, P_B^2$, and localization uncertainty $\sigma_A^2$ and $\sigma_B^2$ the measure is the given as:

$$C_{AB}(\alpha,\beta) = \frac{XYZ}{N_A N_B} = \frac{1}{2\pi}\frac{XY}{N_A N_B}\sum_{i=1}^{N_A}\sum_{j=1}^{N_B}\frac{w_{ij}}{\sigma_{ij}^2}\exp -\frac{(\alpha - x_{ij})^2 + (\beta - y_{ij})^2}{2\sigma_{ij}^2}, \tag{42}$$

where $\sigma_{ij} = \sigma_i^2 + \sigma_j^2$ and $w_{ij}$ is a weight value set to the inverse of the local density, the vector $< x_{ij}, y_{ij} >$ describes the displacement vector from $P_A^2[i]$ to $P_B^2[j]$. An aggregate function is also proposed for a radial distance r. From the definition, this is clearly an asymmetric measure. Computational complexity depends, in worst case this is an $O(N^2)$ algorithm, but an intelligent encoding with e.g. KD-Trees and a radial version can reduce this to $O(RN \log N)$. The weight density vector betrays the reliance on an interpretation of what 'dense' means, and what a neighbourhood is. Apart from particle tracking, the method is also derived for 'point-set' distances, which in this case refers to using the nearest neighbourhood distance from a single point in $P_A$ to all points in $P_B$. Such a point to point mapping can be sensitive to perturbations. The mapping, unaggregated, is given by:

$$f_{DBEM,SR_{\downarrow}} :< P_1^3, P_2^3 >\rightarrow< P_3^3 > . \tag{43}$$

In validation experiments both simulated, real, and phantom (DNA origami) data was used. Colocalization is interpreted by first applying a point cloud segmentation for the 'point to set' distance analysis, and then interpreting the resulting cross correlation distance distribution.

### 7.13. Interaction Factor

Bermudez et al [128] introduce the IF, defined on 2D images, in SMLM data, where such images can be generated from point cloud data. The idea is based on contrasting against randomization (Section 3.8). In practice, objects, in image form, are segmented, then their location is randomized. Overlap of actual objects is then contrasted to the random probability of overlap.

$$P\frac{\sum_{k=1}^{n}\frac{p_k^{(0)}}{1-(1-p_k^{(0)})\times f}}{n}. \tag{44}$$

Here, $f$ is the interaction factor, P is the fraction of overlapping clusters of a reference color, $p_k^(0)$ is the probability that the k'th cluster overlaps in a randomization experiment and n is the total number of clusters. From the equation (Eqn 44) above the interaction factor $f$ can be solved for. The choice of a randomized experiment is always subtle and critical at the same time, but one reference here is that such an experiment should have an IF value of 0. The authors then subdivide the range of IF from no interaction (0-0.3), to low (0.3-0.6), to interaction (0.6-1.0). Interaction here has to be overlap, so interaction scale I. By decreasing precision and lowering segmentation, scale II could be quantified as well. This is an asymmetric measure, indirect, as it requires segmentation, here using Otsu, and image projection, and has no confidence values, though in principle it is possible to add those. The IF function is also reported to behave non linear in function of interaction scenarios.

$$f_{IF,SR_{\downarrow}} :< V_2^2, V_2^2 >\rightarrow< V_3 > . \tag{45}$$

Validation is done on in-silico data as well as colocalizing DNA damage repair proteins. Complexity depends on the randomization scheme, with other operations being linear $O(N)$.

### 7.14. Chromosome-contact - Nir's entanglement score for co-occurrence

Nir's entanglement score (NIR) [67] is developed specifically for the use case of chromosome based analysis using SMLM. After preprocessing with DBSCAN [65], point cloud clusters are transformed into tetrahedra using the alpha shape algorithm. Briefly, alpha shapes refer to filtered subset of tetrahedra from a Delaunay triangulation, and are useful to restrict the triangulated shape to one that is easier to derive semantically important shape features. The alpha threshold radius here was defined based on semantic conditions. Spatial overlap is then determined by measuring the directed pairwise spatial intersection of those alpha shapes. In addition to the point cloud based analysis, Nir et al.[67] use an image based representation as well, where first a pixellated density map is reconstructed from binned localization counts, subsequently convoluted with Gaussian filter to transform to a continuous smoothed representation of the density function. This is a common technique in SRM point cloud to image representations, comparable with estimating a kernel density function from a histogram. Next, the distance was computed between centers of mass in this representation. This distance was corrected using genomic reference data. A second measure, 'entanglement', was computed as the

overlap between isocontour thresholded density maps. In total, this results in 3 mappings:

$$f_{nir_\alpha,T,SR_\downarrow} :< P_1^3, P_2^3 >\rightarrow< P_3 > . \quad (46)$$

Alpha shapes can be obtained in $O(N)$, so the complexity is dominated by the 2 Delaunay triangulations $O(N \log N + N^{\frac{d+1}{2}})$. The measure is asymmetric, and indirect, requiring segmentation first.

$$f_{nir_{fuzzy-distance},SR_\uparrow} :< P_1^3, P_2^3 >\rightarrow< V_3^2 > . \quad (47)$$

Complexity of the fuzzy distance is $O(M^2)$ in M modes of the density function (clusters), with clusters localized by peak finding in a $O(N)$.

$$f_{IF,SR_\downarrow} :< V_2^2, V_2^2 >\rightarrow< V_3 > . \quad (48)$$

The entanglement score is asymmetric, and linear.

### *7.15. Congruence coefficient - interacting trajectories*

Nozaki et al [95], study chromatin domains in live cell photoactivation localization microscopy (PALM) [23] SRM, use the combination of a radial basis function (RBF) (Eqn. 49) to segment SRM localizations:

$$rbf(r) = \frac{S}{N-1}\frac{1}{\pi(2r\Delta r + \Delta r)}\frac{1}{N}\sigma_{i=1}^{N}\sigma_{i\neq j}\delta(r - r_{i,j}). \quad (49)$$

where $\Delta r$ is a binning radius and the $\delta_r$ is an r-thresholded indicator function. $r_{i,j}$ is the distance between localizations $r_i$ and $r_j$. The RBF is a local area rescaled variant of Ripley's K function (Eqn. 33). They then correlate movement of the trajectories of RBF-segmented objects across channels with the congruence coefficient (CE) [149]:

$$CE = \frac{\sum_{i,j} x_{i,j}y_{i,j}}{\sqrt{(\sum_{i,j} x_{i,j}^2)}\sqrt{(\sum_{i,j} y_{i,j}^2)}}. \quad (50)$$

It was shown [149] that a multitude of multidimensional analysis methods implicitly optimize CE. This an asymmetric, indirect measure. From the algorithm description it follows that the core computational complexity is determined by nearest neighbour lookup, so an estimate of $O(RN \log N)$ is a good approximation where $R$ is the number of queries and $N$ the point cloud size. The mapping is given by:

$$f_{CE,R,SR_\downarrow} :< P_1^3, P_2^3 >\rightarrow< P_3^2 > . \quad (51)$$

Interaction scale is I to IV, though in practice applied to I-II.

### *7.16. NeNa - precision as interaction*

Endesfelder et al [20] note that while theoretical localization precision can be derived from the photon count and the variance of the fitted PSF, there is a large and variable gap between empirical and theoretical precision. Yet in interaction analysis, a precise distance would rely heavily on this precision. The criterion they propose NeNa, is not a direct interaction method, but because it implicitly looks at distance-based interaction across frames. Frames, here, are the intervals during which spatio-temporally separated emissions are localized. Specifically, they derive the spatial probability distribution of a single emission:

$$p(d_{i,j}) = \frac{d_{i,j}}{2\sigma_s^2}\exp\frac{-d_{i,j}^2}{4\sigma_s^2}. \quad (52)$$

By relying on the multiple blinking phenomenon, where a single emission will be observed several times across frames, the probability function (Eqn. 52) can be fitted, with a correction for false positive nearest neighbours not sourced from the same emission, and the $\sigma_s$ precision can be obtained empirically. While NeNa is not used explicitly in multichannel context, it can be for the I-interaction scale, e.g. co-occurrence, where the probability distance distribution across frames and channels can be informative. Indeed, different scales of colocalization would separate into different distribution modes. Note that while the complexity is in principle for $N$ points $O(N \log N)$, in practice it is $O(N \log M)$ with $M << N$, as the number of localizations per frame ($M$) is several orders of magnitude smaller than $N$. This observation makes NeNa a very fast metric for multichannel or temporal analysis. The mapping is given by:

$$f_{NeNa,SR_\downarrow} :< P_1^4 >\rightarrow< P_2^3 > . \quad (53)$$

It is a directional metric, software is available. NeNa would inspire future probabilistic methods of interaction in STED and SMLM.

### *7.17. Expansion microscopy: EXM*

Expansion microscopy (EXM) [150] is a process where the cell is chemically fixed, labelled, and subsequently expanded by a chemical process to 'scale up' the cellular tissue, rather than improve the optical or localization stages of the acquisition. A clear advantage of EXM approaches is that thick tissue can be studied, which can be problematic in other SRM modalities. In Kunz et al [129] EXM is used to study cristae on mitochondria in up to 3 channels. The key problem in expansion microscopy is determining if the expansion deforms the original structure, but Kunz et al claim a safe isotropic 4x fold increase, and thus a four-fold increase in resolution below the diffraction limit. The method is validated by looking at the cross-section in intensity of 3 channels where, adjacency and overlap are expected from the biology. While computationally simple, this work is included because EXM promises to be powerful modality for future work, and more than two channels are used, with up to four being listed as feasible. The bootstrapped validation of identifying a sub-membrane protein and showing using intensity profiles in EXM that it is adjacent illustrates the chicken-and-egg nature of validation in novel SRM discovery.

$$f_{EXM,SR_=} :< V_1^3, V_2^3, V_3^3 >\rightarrow< V_1^3, V_2^3, V_3^3 > . \quad (54)$$

Complexity is linear, and without extra processing the measure is undirected, though intensity correlation could be leveraged, or FWHM-based approaches. Interaction scales applicable are I+II, though in principle larger scales can be used. However, critical is knowing the deformation at larger scales and ranges. Best possible precision is listed as 30 nm if EXM is combined with SIM.

### 7.18. TRXM: Expansion to nanometer scales

Damstra et al [109] propose tenfold expansion microscopy (TRXM) [109], contrasted to the classical fourfold [150, 129] and review in detail the deformation that occurs in their own proposed approach and related methods, which has important implications for analysis. This work is included because it studies in detail the deformation in function of expansion, which is critical for future interaction analysis methods. The validation was performed using a combination of nanopores, microtubules, and synapse analysis. Notably, the error in EXM in reconstruction of nanopores (20-30%) was markedly smaller in TRXM (8%), these numbers give some baseline to the uncertainty in interaction analysis. The interaction analysis used the Euclidean distance between intensity peaks nearest to segmentation masks, where the intensity peaks offset potential segmentation errors. The interaction scales studied are I-II. The interaction analysis was symmetric, complexity assumed to be linear given that the segmentation details are unclear. This approach can be extended to more than 2 channels, but not performed in this work. The mathematical model is given by:

$$f_{EXM,SR_{\downarrow}} :< V_1^3, V_2^3 >\rightarrow< V_1^3 > . \tag{55}$$

### 7.19. Chromatin tracing - CT

Bintu et al [94] propose a point-cloud based overlap coefficient chromatin overlap tracing (CT) [94] for chromatin tracing. After running DBSCAN, they compute for each pair of clusters $i, j$ with localizations $Q, R$ respectively in channel $k$ and a threshold $T$:

$$CT(P_{ki}, P_{kj}) = \frac{|\{d_q r| \; ||P_{ki}[q] - P_{ki}[r]|| < T \;\; \forall q \in 1, Q, r \in 1, Q\}|}{|P_{ki} \times P_{kj}|} \tag{56}$$

The mapping is given by

$$f_{CT,\theta=T,d_1,d_2SR_{\downarrow}} :< P_1^3, P_2^3 >\rightarrow< P_1^3 > . \tag{57}$$

Complexity is $O(QR)$, or $O(N^2)$, although if the threshold is known an intelligent KD-Tree based approach could limit it to $O(MNlogN)$. This is a symmetric measure, and indirect. Similarity with the Clus-DoC approach is notable, though this coefficient is aimed at thresholded overlap and direct adjacency (I-II). The determination of the threshold can be contrasted with the approach in Mancebo's [126] CCF.

### 7.20. Statistical point cloud similarity as interaction: KS-test for point clouds

Baragilly et al.[100] argue that a problem in interaction analysis in point clouds is that they rely implicitly on the assumption that the two, or more, point clouds come from the same 'space'. A key example where this becomes problematic is when one channel has lower density due to labelling, or drift is worse, or suffers asymmetrically from any of the confounding issues enumerated earlier (Section 3). However, in comparing in silico data to real data this problem also occurs, how 'real' is simulated data? Refining the simulation parameters itself is not enough to ensure point clouds are similar or realistic, and this is a problem for e.g. deep learning-based algorithms that need supervised data. To resolve this, they propose Kolmogorov-Smirnov probability of colocalization (KSP) [100], the $\lambda$ similarity score based on the cumulative discrete density function (cdf) of 2D projected 3D SMLM data. The score itself is based on the Kolmogorov-Smirnov test that outputs a 0 when presented with two cdf's if they are indistinguishable, and a positive scalar and a p-value that indicates the dissimilarity and confidence. The method works by projecting localizations onto a 2D pixel grid, with pixel size varied 30-50 nm, binning localizations, and computing the cdf of the grid. This is a symmetric measure, the complexity depends on the test but is not greater than linear in practice: $O(N)$. The source code is available and the metric is calibrated on T-cell synapse PALM data, though that data is not available. It should be noted that the K-S statistics require a large number of observations to have sufficient power. It is an indirect method. For pixel size $p$, the mapping is:

$$f_{KSP,\theta=pSR_{\downarrow}} :< P_1^3, P_2^3 >\rightarrow< P_1^3 > . \tag{58}$$

### 7.21. Random contrasted colocalization in SMLM (RC)

Åberg et al.[35] continue the work of Helmuth et al [73] in computing the random probability of 2 objects colocalizing in superresolution. While a GUI method was implemented to reproduce the approach of Helmuth et al was released for PALM [111], but without algorithmic advances to tailor to SRM. Along the same lines as Helmuth's, Åberg's method is not an interaction method 'per se', but rather a way to compute the probability of random interaction or colocalization (scale I-II), given a distance threshold, cell shape, and object size and density. The derivation takes in a reference set of objects and a variable set of objects in a cell shape approximated by a cylinder with spherical caps. The computations are further simplified by observing a virtual focal plane at the center, where e.g. edge effects would be minimal. They define colocalization as thresholded distance, with fixed size objects. The random probability of colocalization with at least one object of the other channel is a *non-linear* function, increasing with decreasing cell shape and increasing number of objects, as well as increased colocalization distance $\psi$. The random probability, even for 5 objects, can rapidly exceed 50%. This is an asymmetric measure, that works with locations, so can both work on voxel and point cloud data.

$$f_{RA,\theta=N_A,N_B,\psi SR_{\downarrow}} :< P_1^3, P_2^3 >\rightarrow< P_1^3 > . \tag{59}$$

Complexity is in principle $O(1)$ given that the closed form equations are given, though in practice randomized experiments would need to be performed to verify and calibrate parameters, so $O(RN)$ with $R$ repeats, plus the cost of nearest neighbour distance $O(N \log N)$. The total cost is then likely to be $O(RN \log N)$ Source code is not available, nor is data. It is of interest to leave some of the closed form derivations, for example the probability that 2 objects colocalize in a circle with radius $R$ within distance $\psi$ is given by:

$$\frac{\psi}{R}^2 (1 - \frac{4\psi}{3\pi R}). \tag{60}$$

Without edge effects, that is, objects near the circumference, this is approximately $\frac{\psi}{R}^2$. More complex derivations for projections of 3D to 2D cases, and edge conditions are computed. This work implicitly recognizes the causal problem formulation illustrated in Fig. 5-A).

### 7.22. FIBSEM segmentation

Heinrich et al [102] reconstruct discrete interaction between organelles by segmenting the 4-8 nm precise focused ion beam scanning electron microscopy (FIBSEM). This is a supervised CNN based approach, with distance between discrete organelles defined as interaction, thresholded on a per-organelle basis. Complexity is dominated by the network, so to avoid a biased estimate, is omitted here. Note that a number of pre- and post-processing steps are applied to fine-tune the prediction. Notable is also the illustrative variability in error between organelles, as there is no explicit regularization for inter-organelle contact correctness, only segmentation. The mapping is given by

$$f_{fibsem,\theta=\theta_N,\theta_P(4+)SR_{\downarrow}} :< V_1^3, V_2^3 >\rightarrow< V_1^3 > . \quad (61)$$

This work is at the edge of fluorescence SRM and EM, and included here as a representative of the state-of-the-art in segmentation for interaction. The actual segmentation is a 4-way classification depending on the organelle, for example for ER, lumen and membrane are 2 classes. Postprocessing involves but is not limited to smoothing, connected components, and watershed to disconnect imprecise segmentation output. Code and data are available in the novel N5 format [30].

### 7.23. Organelle-specific segmentation enables many-channel microscopy

While the number of channels in multichannel acquisitions are increasing, it is unmistakably hard to acquire robust and reproducible datasets with more than two channels in fluorescence microscopy. In order to overcome this, Zhanghao et al [103] propose per-organelle trained networks to infer segmentation on 2-channel super-resolved spinning disk microscopy. With this approach, only at most 2 channels need to be acquired, yet up to 12 organelles can be identified. They further report extensively on the expected error (10% pixelwise), and note that cell-wise differences, which are notable in e.g. [102], can be mitigated with minimal transfer learning. Data is acquired by repeated lipid staining of an organelle target with reported high accuracy, then acquiring in 2-channel proprietary SR-enhanced spinning disk microscopy. Full data and source code (supervised), are available.

$$f_{SS,\theta=\theta_N SR_{\uparrow}} :< V_1^3, V_2^3 >\rightarrow< V_1^3, ..., V_{15}^3 > . \quad (62)$$

Complexity is linear in inference, but hard to estimate in training. While the training is not enhanced by colocalization, it is used in validation. Interaction classes that can be studied with this range from I to IV. This is an indirect, asymmetric method.

### 7.24. STED-Resolft tracing of ER-Mito constriction (EMC)

Damenti et al [110] identify ER-mitochondria constriction sites using reversible saturable optical fluorescence transitions (RESOLFT), and more specifically its 3D STED variant. They identify constriction sites based on the FWHM in (claimed) isotropic precision of 50 nm, including temporal observations. Basic image processing (deconvolution and filtering), no extra processing is applied.

$$f_{EMC,\theta=\emptyset} :< V_1^3, V_2^3 >\rightarrow< V_1^3 > . \quad (63)$$

In contrast to the M-Value approach, there is no computation of an interaction score, rather, presence of constrictions is determined by orthogonal cross-sections of intensity profile FWHM of ER and mitochondria. Complexity is O(N) (minus the maximum likelihood estimation (MLE) deconvolution and registration), it is a direct asymmetric method. Code is not released.

### 7.25. Multicolor expansion fluorescence emission difference microscopy to reveal potential organelle contacts - ExFED

expansion fluorescence emission difference microscopy (ExFED) [108] combines multichannel labelling using fluorescence emission difference (FED) with EXM with a claimed resolution of 60 nm (40 nm lateral). FED is selected because its differential usage subtracted confocal PSFs mitigates photobleaching and toxicity. Validation is done using microtubules. Interaction is studied using cross-section FWHM analysis, with a complexity of $O(N)$. The mapping is:

$$f_{exfed,\theta=\emptyset} :< V_1^3, V_2^3 >\rightarrow< V_1^3 > . \quad (64)$$

Unlike EXM and TRXM, here explicit multiple channels are present, so FWHM approaches can work, whereas earlier single channel to multiple organelle segmentation is needed. This is a direct symmetric method.

### 7.26. Declaration of usage of AI tools

AI based tools (WriteFull) were used to correct grammatical errors and to improve the writing, but all semantic and intellectual contributions originate with the authors solely. Note that some non-essential references are omitted due to journal restrictions. Where acronyms for methods are not given by the introducing art, we provide a shorthand for ease of reference.

### 7.27. Index of terms

**Acronyms**

**CLT** Coloc-Tesseler . . . . . 23

**Clus-DoC** Clustering based colocalization . . . . . 23

**CNN** Convolutional neural network . . . . . 13

**CR** Cardinality ratio . . . . . 6

**CRLB** Fréchet-Darmois-Cramér-Rao lower bound . . . . 10

**CT** Chromatin overlap tracing . . . . . 27

**DBEM** Density based enrichment measure . . . . . 24

**DBSCAN** Density-Based Spatial Clustering of Applications with Noise . . . . . 19

**dSTORM** Direct stochastic optical reconstruction microscopy 3

**EM** Electron microscopy . . . . . 3

**ER** Endoplasmic Reticulum . . . . . 3

**ExFED** Expansion fluorescence emission difference microscopy . . . . . 28

**EXM** Expansion microscopy . . . . . 26

**FED** Fluorescence emission difference . . . . . 28

**FIBSEM** Focused ion beam scanning electron microscopy 28

**FRC** Fourier ring correlation . . . . . 10

**FWHM** Full-width half-maximum . . . . . 10

**GF** Getis and Franklin . . . . . 22

**IF** Interaction factor . . . . . 19

**KD-Tree** K-Dimensional Tree . . . . . 19

**KSP** Kolmogorov-Smirnov probability of colocalization . 27

**LCF** Localization correlation framework . . . . . 25

**M-Value** Mitochondria lysosome interaction value . . . . 19

**MCS-DETECT** Membrane Contact Site Detection . . . 22

**MERC** Mitochondria-ER Contact . . . . . 19

**MINFLUX** Minimal photon fluxes . . . . . 10

**MLE** Maximum likelihood estimation . . . . . 28

**NA** Numerical aperture . . . . . 10

**NeNa** Precision as interaction . . . . . 10

**NIR** Nir's entanglement score . . . . . 25

**PALM** Photoactivation localization microscopy . . . . . 26

**PSF** Point spread function . . . . . 10

**RBF** Radial basis function . . . . . 26

**RESOLFT** Reversible saturable optical fluorescence transitions . . . . . 28

**SFP** Separated or split fluorescent probe . . . . . 14

**SIM** Structured illumination microscopy . . . . . 3

**SMLM** Single Molecule Localization Microscopy . . . . . 4

**SNR** Signal to noise ratio . . . . . 13

**SRM** Super Resolution Microscopy . . . . . 1

**SSL** Self-supervised learning . . . . . 21

**STED** Stimulated Emission Depletion . . . . . 3

**TRXM** Tenfold expansion microscopy . . . . . 26

## References


[1] B. Cardoen, H. B. Yedder, A. Sharma, K. C. Chou, I. R. Nabi, G. Hamarneh, ERGO: Efficient Recurrent Graph Optimized Emitter Density Estimation in Single Molecule Localization Microscopy, IEEE Transactions on Medical Imaging 39 (6) (2020) 1942–1956. doi:10.1109/TMI.2019.2962361. 4, 12, 13, 14, 15

[2] B. Cardoen, T. Wong, P. Alan, S. Lee, J. A. Matsubara, I. R. Nabi, G. Hamarneh, SPECHT: Self-tuning Plausibility based object detection Enables quantification of Conflict in Heterogeneous multi-scale microscopy, PLOS ONE 17 (12) (2022) e0276726. doi:10.1371/journal.pone.0276726.
URL https://journals.plos.org/plosone/article?id=10.1371/journal.pone.0276726 4, 13, 14, 15

[3] B. Cardoen, K. R. Vandevoorde, G. Gao, M. Ortiz-Silva, P. Alan, W. Liu, E. Tiliakou, A. W. Vogl, G. Hamarneh, I. R. Nabi, Membrane contact site detection (MCS-DETECT) reveals dual control of rough mitochondria–ER contacts, Journal of Cell Biology 223 (1) (2023) e202206109. doi:10.1083/jcb.202206109.
URL https://doi.org/10.1083/jcb.202206109 4, 11, 13, 14, 15, 18, 19, 20, 22

[4] A. Lee, K. Tsekouras, C. Calderon, C. Bustamante, S. Pressé, Unraveling the Thousand Word Picture: An Introduction to Super-Resolution Data Analysis, Chemical Reviews 117 (11) (2017) 7276–7330. doi:10.1021/acs.chemrev.6b00729.
URL https://doi.org/10.1021/acs.chemrev.6b00729 3, 4, 5, 6

[5] P. Rodríguez-Sevilla, S. A. Thompson, D. Jaque, Multichannel Fluorescence Microscopy: Advantages of Going beyond a Single Emission, Advanced NanoBiomed Research 2 (5) (2022) 2100084. doi:10.1002/anbr.202100084.
URL https://onlinelibrary.wiley.com/doi/abs/10.1002/anbr.202100084 3, 4, 5, 6

[6] L. Schermelleh, A. Ferrand, T. Huser, C. Eggeling, M. Sauer, O. Biehlmaier, G. P. C. Drummen, Super-resolution microscopy demystified, Nature Cell Biology 21 (1) (2019) 72–84. doi:10.1038/s41556-018-0251-8.
URL https://www.nature.com/articles/s41556-018-0251-8 3

[7] S. W. Hell, J. Wichmann, Breaking the diffraction resolution limit by stimulated emission: stimulated-emission-depletion fluorescence microscopy, Optics Letters 19 (11) (1994) 780–782, publisher: Optical Society of America. 3

[8] F. Schueder, F. Rivera-Molina, M. Su, Z. Marin, P. Kidd, J. E. Rothman, D. Toomre, J. Bewersdorf, Unraveling cellular complexity with transient adapters in highly multiplexed super-resolution imaging, Cell 187 (7) (2024) 1769–1784.e18. doi:10.1016/j.cell.2024.02.033. 3, 20

[9] H. Nyquist, Certain Topics in Telegraph Transmission Theory, Transactions of the American Institute of Electrical Engineers 47 (2) (1928) 617–644. doi:10.1109/T-AIEE.1928.5055024.
URL http://ieeexplore.ieee.org/document/5055024/ 3, 10, 14

[10] E. T. Whittaker, XVIII.—On the Functions which are represented by the Expansions of the Interpolation-Theory, Proceedings of the Royal Society of Edinburgh 35 (1915) 181–194. doi:10.1017/S0370164600017806.
URL https://www.cambridge.org/core/product/identifier/S0370164600017806/type/journal_article 3, 10, 14

[11] H. Herce, C. Casas-Delucchi, M. Cardoso, New image colocalization coefficient for fluorescence microscopy to quantify (bio-)molecular interactions, Journal of Microscopy 249 (3) (2013) 184–194. doi:10.1111/jmi.12008.
URL https://onlinelibrary.wiley.com/doi/abs/10.1111/jmi.12008 3, 6

[12] J. Adler, I. Parmryd, Quantifying colocalization: The case for discarding the Manders overlap coefficient, Cytometry Part A 99 (9) (2021) 910–920. doi:10.1002/cyto.a.24336.
URL https://onlinelibrary.wiley.com/doi/abs/10.1002/cyto.a.24336 3

[13] J. Rossy, E. Cohen, K. Gaus, D. M. Owen, Method for co-cluster analysis in multichannel single-molecule localisation data, Histochemistry and Cell Biology 141 (6) (2014) 605–612. doi:10.1007/s00418-014-1208-z. 3, 14, 18, 19, 20, 22

[14] P. Wofgang, Über den Zusammenhang des Abschlusses der Elektronengruppen im Atom mit der Komplexstruktur der Spektren | SpringerLink, Einf{\"u}hr. Orig 229 (1925) 765–783.
URL https://link.springer.com/article/10.1007/BF02980631 3

[15] J. S. Aaron, A. B. Taylor, T.-L. Chew, Image co-localization – co-occurrence versus correlation, Journal of Cell Science 131 (3) (2018) jcs211847. doi:10.1242/jcs.211847. 3, 4, 6

[16] T. Lagache, N. Sauvonnet, L. Danglot, J.-C. Olivo-Marin, Statistical analysis of molecule colocalization in bioimaging, Cytometry Part A 87 (6) (2015) 568–579, publisher: Wiley Online Library. 3, 4, 6

[17] Y. Huo, W. Sun, T. Shi, S. Gao, M. Zhuang, The MFN1 and MFN2 mitofusins promote clustering between mitochondria and peroxisomes, Communications Biology 5 (May 2022). doi:10.1038/s42003-022-03377-x. 3

[18] J. Ma, J. Tang, A review for dynamics in neuron and neuronal network, Nonlinear Dynamics 89 (3) (2017) 1569–1578. doi:10.1007/s11071-017-3565-3.
URL https://doi.org/10.1007/s11071-017-3565-3 3

[19] N. Chenouard, I. Smal, F. de Chaumont, M. Maška, I. F. Sbalzarini, Y. Gong, J. Cardinale, C. Carthel, S. Coraluppi, M. Winter, A. R. Cohen, W. J. Godinez, K. Rohr, Y. Kalaidzidis, L. Liang, J. Duncan, H. Shen, Y. Xu, K. E. G. Magnusson, J. Jaldén, H. M. Blau, P. Paul-Gilloteaux, P. Roudot, C. Kervrann, F. Waharte, J.-Y. Tinevez, S. L. Shorte, J. Willemse, K. Celler, G. P. van Wezel, H.-W. Dan, Y.-S. Tsai, C. O. de Solórzano, J.-C. Olivo-Marin, E. Meijering, Objective comparison of particle tracking methods, Nature Methods 11 (3) (2014) 281–289. doi:10.1038/nmeth.2808.
URL https://www.nature.com/articles/nmeth.2808 4, 6

[20] U. Endesfelder, M. Heilemann, Direct Stochastic Optical Reconstruction Microscopy (dSTORM), in: Methods in molecular biology (Clifton, N.J.), Vol. 1251, Clifton, N.J., 2015, pp. 263–276, iSSN: 1940-6029. doi:10.1007/978-1-4939-2080-8_14.
URL http://www.ncbi.nlm.nih.gov/pubmed/25391804 4, 11, 14, 24, 26

[21] L. MacDonald, G. Baldini, B. Storrie, Does super-resolution fluorescence microscopy obsolete previous microscopic approaches to protein co-localization, Methods in Molecular Biology 1270 (2015) 255–275. doi:10.1007/978-1-4939-2309-0_19.
URL https://europepmc.org/article/med/25702123 4, 14

[22] Y.-L. Wu, A. Tschanz, L. Krupnik, J. Ries, Quantitative Data Analysis in Single-Molecule Localization Microscopy, Trends in Cell Biology 30 (11) (2020) 837–851. doi:10.1016/j.tcb.2020.07.005.
URL https://www.sciencedirect.com/science/article/pii/S096289242030146X 4, 6

[23] E. Betzig, G. H. Patterson, R. Sougrat, O. W. Lindwasser, S. Olenych, J. S. Bonifacino, M. W. Davidson, J. Lippincott-Schwartz, H. F. Hess, Imaging intracellular fluorescent proteins at nanometer resolution, Science (New York, N.Y.) 313 (5793) (2006) 1642–1645. doi:10.1126/science.1127344. 4, 26

[24] O. Faklaris, L. Bancel-Vallée, A. Dauphin, B. Monterroso, P. Frère, D. Geny, T. Manoliu, S. de Rossi, F. P. Cordelières, D. Schapman, R. Nitschke, J. Cau, T. Guilbert, Quality assessment in light microscopy for routine use through simple tools and robust metrics, Journal of Cell Biology 221 (11) (2022) e202107093. doi:10.1083/jcb.202107093.
URL https://doi.org/10.1083/jcb.202107093 4, 6, 14

[25] I. M. Khater, I. R. Nabi, G. Hamarneh, A Review of Super-Resolution Single-Molecule Localization Microscopy Cluster Analysis and Quantification Methods, Patterns 1 (3) (2020) 100038. doi:10.1016/j.patter.2020.100038.
URL https://www.sciencedirect.com/science/article/pii/S266638992030043X 4, 13, 21

[26] Y. Hyun, D. Kim, Recent development of computational cluster analysis methods for single-molecule localization microscopy images, Computational and Structural Biotechnology Journal 21 (2023) 879–888. doi:10.1016/j.csbj.2023.01.006.
URL https://www.sciencedirect.com/science/article/pii/S2001037023000077 4, 6

[27] D. J. Nieves, J. A. Pike, F. Levet, D. J. Williamson, M. Baragilly, S. Oloketuyi, A. de Marco, J. Griffié, D. Sage, E. A. K. Cohen, J.-B. Sibarita, M. Heilemann, D. M. Owen, A framework for evaluating the performance of SMLM cluster analysis algorithms, Nature Methods 20 (2) (2023) 259–267. doi:10.1038/s41592-022-01750-6.
URL https://www.nature.com/articles/s41592-022-01750-6 4, 6

[28] C. S. Hansel, M. N. Holme, S. Gopal, M. M. Stevens, Advances in high-resolution microscopy for the study of intracellular interactions with biomaterials, Biomaterials 226 (2020) 119406. doi:10.1016/j.biomaterials.2019.119406.
URL https://www.sciencedirect.com/science/article/pii/S0142961219305058 6

[29] D. Sage, T.-A. Pham, H. Babcock, T. Lukes, T. Pengo, J. Chao, R. Velmurugan, A. Herbert, A. Agrawal, S. Colabrese, A. Wheeler, A. Archetti, B. Rieger, R. Ober, G. M. Hagen, J.-B. Sibarita, J. Ries, R. Henriques, M. Unser, S. Holden, Super-resolution fight club: assessment of 2D and 3D single-molecule localization microscopy software, Nature Methods 16 (5) (2019) 387–395. doi:10.1038/s41592-019-0364-4.
URL https://www.nature.com/articles/s41592-019-0364-4 6

[30] S. Saalfeld, I. Pisarev, P. Hanslovsky, A. Champion, C. Rueden, J. Bogovic, M. Kittisopikul, Jakirkham, saalfeldlab/n5: n5-2.5.1 (May 2022). doi:10.5281/ZENODO.6578232.
URL https://zenodo.org/record/6578232 6, 19, 28

[31] D. E. Gottschling, T. Nyström, The Upsides and Downsides of Organelle Interconnectivity, Cell 169 (1) (2017) 24–34. doi:10.1016/j.cell.2017.02.030.
URL https://www.sciencedirect.com/science/article/pii/S0092867417302453 10

[32] I. R. Nabi, B. Cardoen, I. M. Khater, G. Gao, T. H. Wong, G. Hamarneh, AI-based analysis of super-resolution microscopy: Biological discovery in the absence of ground truth, Arxiv 1 (1) (2023). doi:10.48550/ARXIV.2305.17193.
URL https://arxiv.org/abs/2305.17193 10, 14

[33] G. G. Stokes (Ed.), On the Effect of the Internal Friction of Fluids on the Motion of Pendulums, Vol. 3 of Cambridge Library Collection - Mathematics, Cambridge University Press, Cambridge, 2009. doi:10.1017/CBO9780511702266.002.
URL https://www.cambridge.org/core/books/mathematical-and-physical-papers/on-the-effect-of-the-internal-friction-of-fluids-on-the-motion-11038EBC1E2D897D9E5B1297C9AE5D99 10

[34] E. M. Purcell, Life at low Reynolds number, American Journal of Physics 45 (1) (1977) 3–11. doi:10.1119/1.10903.
URL https://aapt.scitation.org/doi/10.1119/1.10903 10

[35] C. Åberg, A. Robinson, Single-molecule localisation microscopy: accounting for chance co-localisation between foci in bacterial cells, European Biophysics Journal 50 (7) (2021) 941–950. doi:10.1007/s00249-021-01555-z.

URL https://doi.org/10.1007/s00249-021-01555-z 12, 14, 16, 18, 20, 21, 27

[36] L. Carlini, S. J. Holden, K. M. Douglass, S. Manley, Correction of a Depth-Dependent Lateral Distortion in 3D Super-Resolution Imaging, PLoS ONE 10 (11) (2015) e0142949. doi:10.1371/journal.pone.0142949.
URL https://www.ncbi.nlm.nih.gov/pmc/articles/PMC4658163/ 11, 12, 14

[37] P. Fox-Roberts, R. Marsh, K. Pfisterer, A. Jayo, M. Parsons, S. Cox, Local dimensionality determines imaging speed in localization microscopy, Nature Communications 8 (2017) 13558. doi:10.1038/ncomms13558.
URL https://www.ncbi.nlm.nih.gov/pmc/articles/PMC5241698/ 12, 13, 14, 15

[38] M. Fréchet, Sur l'extension de certaines evaluations statistiques au cas de petits echantillons, Revue de l'Institut International de Statistique / Review of the International Statistical Institute 11 (3/4) (1943) 182. doi:10.2307/1401114.
URL https://www.jstor.org/stable/1401114?origin=crossref 10

[39] J. Willems, H. D. MacGillavry, A coordinate-based co-localization index to quantify and visualize spatial associations in single-molecule localization microscopy, Scientific Reports 12 (1) (2022) 4676. doi:10.1038/s41598-022-08746-4.
URL https://www.nature.com/articles/s41598-022-08746-4 10, 14, 17, 18, 19, 20, 24

[40] J. Schnitzbauer, Y. Wang, S. Zhao, M. Bakalar, T. Nuwal, B. Chen, B. Huang, Correlation analysis framework for localization-based superresolution microscopy, Proceedings of the National Academy of Sciences 115 (13) (2018) 3219–3224. doi:10.1073/pnas.1711314115.
URL http://www.ncbi.nlm.nih.gov/pubmed/29531072 10, 15, 17, 18, 19, 20, 25

[41] N. Banterle, K. H. Bui, E. A. Lemke, M. Beck, Fourier ring correlation as a resolution criterion for super-resolution microscopy, Journal of Structural Biology 183 (3) (2013) 363–367, publisher: Academic Press. doi:10.1016/J.JSB.2013.05.004.
URL https://www.sciencedirect.com/science/article/pii/S1047847713001184 10

[42] M. Van Heel, M. Schatz, Reassessing the Revolution's Resolutions, Arxiv (Nov. 2017). doi:10.1101/224402.
URL https://www.biorxiv.org/content/10.1101/224402v1 10, 14

[43] R. E. Thompson, D. R. Larson, W. W. Webb, Precise Nanometer Localization Analysis for Individual Fluorescent Probes, Biophysical Journal 82 (5) (2002) 2775–2783. doi:10.1016/S0006-3495(02)75618-X.
URL https://www.cell.com/biophysj/abstract/S0006-3495(02)75618-X 10, 14

[44] U. Endesfelder, S. Malkusch, F. Fricke, M. Heilemann, A simple method to estimate the average localization precision of a single-molecule localization microscopy experiment, Histochemistry and Cell Biology 141 (6) (2014) 629–638. doi:10.1007/s00418-014-1192-3.
URL https://doi.org/10.1007/s00418-014-1192-3 11, 18, 20

[45] H. Mazidi, T. Ding, A. Nehorai, M. D. Lew, Quantifying accuracy and heterogeneity in single-molecule super-resolution microscopy, Nature Communications 11 (1) (2020) 6353. doi:10.1038/s41467-020-20056-9. 11, 13, 14

[46] C. He, Z. Zhan, C. Li, X. Sun, Y. Liu, C. Kuang, X. Liu, Effects of optical aberrations on localization of MINFLUX super-resolution microscopy, Optics Express 30 (26) (2022) 46849–46860. doi:10.1364/OE.475425.
URL https://opg.optica.org/oe/abstract.cfm?uri=oe-30-26-46849 11, 14

[47] M. E. Siemons, L. C. Kapitein, S. Stallinga, Axial accuracy in localization microscopy with 3D point spread function engineering, Optics Express 30 (16) (2022) 28290–28300. doi:10.1364/OE.461750.
URL https://opg.optica.org/oe/abstract.cfm?uri=oe-30-16-28290 11, 14

[48] B. C. Coles, S. E. D. Webb, N. Schwartz, D. J. Rolfe, M. Martin-Fernandez, V. L. Schiavo, Characterisation of the effects of optical aberrations in single molecule techniques, Biomedical Optics Express 7 (5) (2016) 1755–1767. doi:10.1364/BOE.7.001755.
URL https://opg.optica.org/boe/abstract.cfm?uri=boe-7-5-1755 11, 14

[49] R. Tafteh, D. R. L. Scriven, E. D. W. Moore, K. C. Chou, Single molecule localization deep within thick cells; a novel super-resolution microscope, Journal of Biophotonics 9 (1-2) (2016) 155–160. doi:10.1002/jbio.201500140.
URL https://onlinelibrary.wiley.com/doi/abs/10.1002/jbio.201500140 13

[50] M. J. Wester, D. J. Schodt, H. Mazloom-Farsibaf, M. Fazel, S. Pallikkuth, K. A. Lidke, Robust, fiducial-free drift correction for super-resolution imaging, Scientific Reports 11 (1) (2021) 23672. doi:10.1038/s41598-021-02850-7.
URL https://www.nature.com/articles/s41598-021-02850-7 13, 14

[51] Y. Wang, J. Schnitzbauer, Z. Hu, X. Li, Y. Cheng, Z.-L. Huang, B. Huang, Localization events-based sample drift correction for localization microscopy with redundant cross-correlation algorithm, Optics Express 22 (13) (2014) 15982–15991. doi:10.1364/OE.22.015982.
URL https://opg.optica.org/oe/abstract.cfm?uri=oe-22-13-15982 13, 14

[52] A. Elmokadem, J. Yu, Optimal Drift Correction for Superresolution Localization Microscopy with Bayesian Inference, Biophysical JournalISBN: 1542-0086 (Electronic)\r0006-3495 (Linking) (2015). doi:10.1016/j.bpj.2015.09.017. 13, 14

[53] J. Cnossen, T. J. Cui, C. Joo, C. Smith, Drift correction in localization microscopy using entropy minimization, Optics Express 29 (18) (2021) 27961–27974. doi:10.1364/OE.426620.
URL https://opg.optica.org/oe/abstract.cfm?uri=oe-29-18-27961 13, 14

[54] J. Lu, J. Öfverstedt, J. Lindblad, N. Sladoje, Is image-to-image translation the panacea for multimodal image registration? A comparative study, PLOS ONE 17 (11) (2022) e0276196. doi:10.1371/journal.pone.0276196.
URL https://journals.plos.org/plosone/article?id=10.1371/journal.pone.0276196 13, 14

[55] J. A. Bogovic, P. Hanslovsky, A. Wong, S. Saalfeld, Robust registration of calcium images by learned contrast synthesis, in: 2016 IEEE 13th International Symposium on Biomedical Imaging (ISBI), 2016, pp. 1123–1126, iSSN: 1945-8452. doi:10.1109/ISBI.2016.7493463. 13, 14

[56] R. J. Marsh, K. Pfisterer, P. Bennett, L. M. Hirvonen, M. Gautel, G. E. Jones, S. Cox, Artifact-free high-density localization microscopy analysis, Nature Methods 15 (9) (2018) 689–692. doi:10.1038/s41592-018-0072-5.
URL https://www.nature.com/articles/s41592-018-0072-5 13, 14

[57] H. Heydarian, M. Joosten, A. Przybylski, F. Schueder, R. Jungmann, B. v. Werkhoven, J. Keller-Findeisen, J. Ries, S. Stallinga, M. Bates, B. Rieger, 3D particle averaging and detection of macromolecular symmetry in localization microscopy, Nature Communications 12 (1) (2021) 2847. doi:10.1038/s41467-021-22006-5. 13, 14

[58] W. Wang, H. Heydarian, T. A. P. M. Huijben, S. Stallinga, B. Rieger, Joint registration of multiple point clouds for fast particle fusion in localization microscopy, Bioinformatics 38 (12) (2022) 3281–3287. doi:10.1093/bioinformatics/btac320.
URL https://www.ncbi.nlm.nih.gov/pmc/articles/PMC9191212/ 13, 14

[59] G. D. Evangelidis, R. Horaud, Joint Alignment of Multiple Point Sets with Batch and Incremental Expectation-Maximization, IEEE Transactions on Pattern Analysis and Machine Intelligence 40 (6) (2018) 1397–1410. doi:10.1109/TPAMI.2017.2717829. 13, 14

[60] L. G. Jensen, T. Y. Hoh, D. J. Williamson, J. Griffié, D. Sage, P. Rubin-Delanchy, D. M. Owen, Correction of multiple-blinking artifacts in photoactivated localization microscopy, Nature Methods 19 (5) (2022) 594–602. doi:10.1038/s41592-022-01463-w. 13, 14

[61] T. A. P. M. Huijben, H. Heydarian, A. Auer, F. Schueder, R. Jungmann, S. Stallinga, B. Rieger, Detecting structural heterogeneity in single-molecule localization microscopy data, Nature Communications 12 (1) (2021) 3791. doi:10.1038/s41467-021-24106-8. 13, 16, 20

[62] I. M. Khater, F. Meng, T. H. Wong, I. R. Nabi, G. Hamarneh, Super resolution network analysis defines the molecular architecture of Caveo-

lae and Caveolin-1 scaffolds, Scientific Reports 8 (1) (2018) 1–15, publisher: Nature Publishing Group. 13

[63] P. Annibale, S. Vanni, M. Scarselli, U. Rothlisberger, A. Radenovic, Identification of clustering artifacts in photoactivated localization microscopy, Nature Methods 8 (7) (2011) 527–528. doi:10.1038/nmeth.1627.
URL https://www.nature.com/articles/nmeth.1627 13, 14, 15

[64] I. Costello, S. Cox, Analysing errors in single-molecule localisation microscopy, The International Journal of Biochemistry & Cell Biology 134 (2021) 105931. doi:10.1016/j.biocel.2021.105931. 13, 14, 15

[65] M. Ester, H.-P. Kriegel, J. Sander, X. Xu, A density-based algorithm for discovering clusters in large spatial databases with noise, in: Proceedings of the Second International Conference on Knowledge Discovery and Data Mining, KDD'96, AAAI Press, Portland, Oregon, 1996, pp. 226–231. 13, 19, 25

[66] S. V. Pageon, P. R. Nicovich, M. Mollazade, T. Tabarin, K. Gaus, Clus-DoC: a combined cluster detection and colocalization analysis for single-molecule localization microscopy data, Molecular Biology of the Cell 27 (22) (2016) 3627–3636. doi:10.1091/mbc.E16-07-0478.
URL https://www.ncbi.nlm.nih.gov/pmc/articles/PMC5221594/ 13, 14, 18, 19, 21, 23

[67] G. Nir, I. Farabella, C. P. Estrada, C. G. Ebeling, B. J. Beliveau, H. M. Sasaki, S. D. Lee, S. C. Nguyen, R. B. McCole, S. Chattoraj, J. Erceg, J. A. Abed, N. M. C. Martins, H. Q. Nguyen, M. A. Hannan, S. Russell, N. C. Durand, S. S. P. Rao, J. Y. Kishi, P. Soler-Vila, M. D. Pierro, J. N. Onuchic, S. P. Callahan, J. M. Schreiner, J. A. Stuckey, P. Yin, E. L. Aiden, M. A. Marti-Renom, C.-t. Wu, Walking along chromosomes with super-resolution imaging, contact maps, and integrative modeling, PLOS Genetics 14 (12) (2018) e1007872. doi:10.1371/journal.pgen.1007872.
URL https://journals.plos.org/plosgenetics/article?id=10.1371/journal.pgen.1007872 13, 14, 18, 19, 25

[68] X. Chai, Q. Ba, G. Yang, Characterizing robustness and sensitivity of convolutional neural networks for quantitative analysis of mitochondrial morphology, Quantitative Biology 6 (4) (2018) 344–358. doi:10.1007/s40484-018-0156-3.
URL https://journal.hep.com.cn/qb/EN/10.1007/s40484-018-0156-3 13, 14, 15

[69] F. Levet, E. Hosy, A. Kechkar, C. Butler, A. Beghin, D. Choquet, J.-B. Sibarita, SR-Tesseler: a method to segment and quantify localization-based super-resolution microscopy data, Nature Methods 12 (11) (2015) 1065–1071. doi:10.1038/nmeth.3579.
URL http://www.ncbi.nlm.nih.gov/pubmed/26344046 13, 14

[70] A. Benfenati, upU-Net Approaches for Background Emission Removal in Fluorescence Microscopy, Journal of Imaging 8 (5) (2022) 142. doi:10.3390/jimaging8050142. 13

[71] A. G. e. a. Vecchiarelli, Membrane-bound MinDE complex acts as a toggle switch that drives Min oscillation coupled to cytoplasmic depletion of MinD, Proceedings of the National Academy of Sciences 113 (11) (2016) E1479–E1488, publisher: National Acad Sciences. 13, 15

[72] S. Irgen-Gioro, S. Yoshida, V. Walling, S. Chong, Fixation can change the appearance of phase separation in living cells, eLife 11 (2022) e79903. doi:10.7554/eLife.79903.
URL https://elifesciences.org/articles/79903 13

[73] J. A. Helmuth, G. Paul, I. F. Sbalzarini, Beyond co-localization: Inferring spatial interactions between sub-cellular structures from microscopy images, BMC Bioinformatics 11 (2010) 1–12. doi:10.1186/1471-2105-11-372. 13, 14, 20, 21, 27

[74] F. Levet, G. Julien, R. Galland, C. Butler, A. Beghin, A. Chazeau, P. Hoess, J. Ries, G. Giannone, J.-B. Sibarita, A tessellation-based colocalization analysis approach for single-molecule localization microscopy, Nature Communications 10 (1) (2019) 2379. doi:10.1038/s41467-019-10007-4.
URL https://www.nature.com/articles/s41467-019-10007-4 14, 15, 16, 18, 19, 20, 23

[75] D. J. Metcalf, R. Edwards, N. Kumarswami, A. E. Knight, Test Samples for Optimizing STORM Super-Resolution Microscopy, Journal of Visualized Experiments 1 (79) (2013) 50579. doi:10.3791/50579.
URL https://www.jove.com/t/50579/test-samples-for-optimizing-storm-super--resolution-microscopy 14

[76] A. Durand, T. Wiesner, M.-A. Gardner, L.-E. Robitaille, A. Bilodeau, C. Gagne, P. De Koninck, F. Lavoie-Cardinal, A machine learning approach for online automated optimization of super-resolution optical microscopy, Nature Communications 9 (1) (2018) 5247, publisher: Nature Publishing Group. doi:10.1038/s41467-018-07668-y.
URL http://www.nature.com/articles/s41467-018-07668-y 14

[77] P. Verzelli, A. Nold, C. Sun, M. Heilemann, E. M. Schuman, T. Tchumatchenko, Unbiased choice of global clustering parameters for single-molecule localization microscopy, Scientific Reports 12 (1) (2022) 22561. doi:10.1038/s41598-022-27074-1.
URL https://www.nature.com/articles/s41598-022-27074-1 14

[78] B. Cardoen, H. B. Yedder, S. Lee, I. R. Nabi, G. Hamarneh, Log-Paradox: Necessary and sufficient conditions for confounding statistically significant pattern reversal under the log-transform, Arxiv 1 (1), arXiv:2302.04780 [math, stat] (Feb. 2023). doi:10.48550/arXiv.2302.04780.
URL http://arxiv.org/abs/2302.04780 14, 15, 16

[79] A. Zimek, E. Schubert, H.-P. Kriegel, A survey on unsupervised outlier detection in high-dimensional numerical data, Statistical Analysis and Data Mining: The ASA Data Science Journal 5 (5) (2012) 363–387, publisher: Wiley Online Library. 14, 15

[80] B. Ruszczycki, T. Bernas, Quality of biological images, reconstructed using localization microscopy data, Bioinformatics (Oxford, England) 34 (5) (2018) 845–852. doi:10.1093/bioinformatics/btx597. 14, 16

[81] A. C. Descloux, K. S. Grußmayer, A. Radenovic, Parameter-free rendering of single-molecule localization microscopy data for parameter-free resolution estimation, Communications Biology 4 (1) (2021) 550. doi:10.1038/s42003-021-02086-1. 14, 16

[82] A. L. Jousselme, P. Maupin, Distances in evidence theory: Comprehensive survey and generalizations, International Journal of Approximate Reasoning 53 (2) (2012) 118–145, publisher: Elsevier Inc. doi:10.1016/j.ijar.2011.07.006.
URL http://dx.doi.org/10.1016/j.ijar.2011.07.006 14

[83] J. Chao, S. Ram, A. V. Abraham, E. S. Ward, R. J. Ober, A resolution measure for three-dimensional microscopy, Optics communications 282 (9) (2009) 1751–1761. doi:10.1016/j.optcom.2009.01.062.
URL https://www.ncbi.nlm.nih.gov/pmc/articles/PMC2753980/ 14

[84] E. A. Mukamel, M. J. Schnitzer, Unified Resolution Bounds for Conventional and Stochastic Localization Fluorescence Microscopy, Physical Review Letters 109 (16) (2012) 168102. doi:10.1103/PhysRevLett.109.168102.
URL https://link.aps.org/doi/10.1103/PhysRevLett.109.168102 14

[85] J. Ma, J. Zhao, J. Tian, A. L. Yuille, Z. Tu, Robust Point Matching via Vector Field Consensus, IEEE Transactions on Image Processing 23 (4) (2014) 1706–1721. doi:10.1109/TIP.2014.2307478. 14

[86] M. van Heel, M. Schatz, Fourier shell correlation threshold criteria, Journal of Structural Biology 151 (3) (2005) 250–262. doi:10.1016/j.jsb.2005.05.009.
URL https://www.sciencedirect.com/science/article/pii/S1047847705001292 14

[87] J. Jonsson, B. L. Cheeseman, S. Maddu, K. Gonciarz, I. F. Sbalzarini, Parallel Discrete Convolutions on Adaptive Particle Representations of Images, IEEE Transactions on Image Processing 31 (2022) 4197–4212. doi:10.1109/TIP.2022.3181487. 14, 19

[88] T. Novák, T. Gajdos, J. Sinkó, G. Szabó, M. Erdélyi, TestSTORM: Versatile simulator software for multimodal super-resolution localization fluorescence microscopy, Scientific Reports 7 (1) (2017) 951, publisher: Nature Publishing Group. doi:10.1038/s41598-017-01122-7.
URL http://www.nature.com/articles/s41598-017-01122-7 14

[89] V. Venkataramani, F. Herrmannsdörfer, M. Heilemann, T. Kuner, SuReSim: simulating localization microscopy experiments from ground truth models, Nature Methods 13 (4) (2016) 319–321. doi:10.1038/nmeth.3775. 14

[90] W. Liu, H. Duan, D. Zhang, X. Zhang, Q. Luo, T. Xie, H. Yan, L. Peng, Y. Hu, L. Liang, G. Zhao, Z. Xie, J. Hu, Concepts and

Application of DNA Origami and DNA Self-Assembly: A Systematic Review, Applied Bionics and Biomechanics 2021 (2021) 1–15. doi:10.1155/2021/9112407.
URL https://www.hindawi.com/journals/abb/2021/9112407/ 14

[91] F. M. Richards, ON THE ENZYMIC ACTIVITY OF SUBTILISIN-MODIFIED RIBONUCLEASE, Proceedings of the National Academy of Sciences 44 (2) (1958) 162–166. doi:10.1073/pnas.44.2.162.
URL https://pnas.org/doi/full/10.1073/pnas.44.2.162 14

[92] J. V. Thevathasan, M. Kahnwald, K. Cieśliński, P. Hoess, S. K. Peneti, M. Reitberger, D. Heid, K. C. Kasuba, S. J. Hoerner, Y. Li, Y.-L. Wu, M. Mund, U. Matti, P. M. Pereira, R. Henriques, B. Nijmeijer, M. Kueblbeck, V. J. Sabinina, J. Ellenberg, J. Ries, Nuclear pores as versatile reference standards for quantitative superresolution microscopy, Nature Methods 16 (10) (2019) 1045–1053. doi:10.1038/s41592-019-0574-9.
URL https://www.nature.com/articles/s41592-019-0574-9 14

[93] S. Malkusch, U. Endesfelder, J. Mondry, M. Gelléri, P. J. Verveer, M. Heilemann, Coordinate-based colocalization analysis of single-molecule localization microscopy data, Histochemistry and Cell Biology 137 (1) (2012) 1–10. doi:10.1007/s00418-011-0880-5. 14, 18, 19, 20, 22, 23

[94] B. Bintu, L. J. Mateo, J.-H. Su, N. A. Sinnott-Armstrong, M. Parker, S. Kinrot, K. Yamaya, A. N. Boettiger, X. Zhuang, Super-resolution chromatin tracing reveals domains and cooperative interactions in single cells, Science (New York, N.Y.) 362 (6413) (2018) eaau1783. doi:10.1126/science.aau1783. 14, 18, 27

[95] T. Nozaki, R. Imai, M. Tanbo, R. Nagashima, S. Tamura, T. Tani, Y. Joti, M. Tomita, K. Hibino, M. T. Kanemaki, K. S. Wendt, Y. Okada, T. Nagai, K. Maeshima, Dynamic Organization of Chromatin Domains Revealed by Super-Resolution Live-Cell Imaging, Molecular Cell 67 (2) (2017) 282–293.e7. doi:10.1016/j.molcel.2017.06.018.
URL https://linkinghub.elsevier.com/retrieve/pii/S1097276517304458 14, 18, 20, 26

[96] J. Nangreave, D. Han, Y. Liu, H. Yan, DNA origami: a history and current perspective, Current Opinion in Chemical Biology 14 (5) (2010) 608–615. doi:10.1016/j.cbpa.2010.06.182. 14

[97] T. Kleele, T. Rey, J. Winter, S. Zaganelli, D. Mahecic, H. Perreten Lambert, F. P. Ruberto, M. Nemir, T. Wai, T. Pedrazzini, S. Manley, Distinct fission signatures predict mitochondrial degradation or biogenesis, Nature (2021) 1–5doi:10.1038/s41586-021-03510-6.
URL https://www.nature.com/articles/s41586-021-03510-6 14, 15, 16, 17, 18, 19, 22

[98] A. L. Ejdrup, M. D. Lycas, N. Lorenzen, A. Konomi, F. Herborg, K. L. Madsen, U. Gether, A density-based enrichment measure for assessing colocalization in single-molecule localization microscopy data, Nature Communications 13 (1) (2022) 4388. doi:10.1038/s41467-022-32064-y.
URL https://www.nature.com/articles/s41467-022-32064-y 14, 17, 18, 19, 24

[99] W. Zhang, J. Sloan-Lancaster, J. Kitchen, R. P. Trible, L. E. Samelson, LAT: The ZAP-70 Tyrosine Kinase Substrate that Links T Cell Receptor to Cellular Activation, Cell 92 (1) (1998) 83–92. doi:10.1016/S0092-8674(00)80901-0.
URL https://www.sciencedirect.com/science/article/pii/S0092867400809010 15

[100] M. Baragilly, D. J. Nieves, D. J. Williamson, R. Peters, D. M. Owen, Measuring the similarity of SMLM-derived point-clouds (Sep. 2022). doi:10.1101/2022.09.12.507560.
URL https://www.biorxiv.org/content/10.1101/2022.09.12.507560v1 15, 16, 18, 19, 27

[101] A. P. St-Pierre, V. Shikon, D. C. Schneider, Count data in biology—Data transformation or model reformation?, Ecology and Evolution 8 (6) (2018) 3077–3085. doi:10.1002/ece3.3807.
URL https://onlinelibrary.wiley.com/doi/abs/10.1002/ece3.3807 15

[102] L. Heinrich, D. Bennett, D. Ackerman, W. Park, J. Bogovic, N. Eckstein, A. Petruncio, J. Clements, S. Pang, C. S. Xu, J. Funke, W. Korff, H. F. Hess, J. Lippincott-Schwartz, S. Saalfeld, A. V. Weigel, Whole-cell organelle segmentation in volume electron microscopy, Nature 599 (7883) (2021) 141–146. doi:10.1038/s41586-021-03977-3.
URL https://www.nature.com/articles/s41586-021-03977-3 15, 16, 17, 18, 19, 20, 28

[103] K. Zhanghao, M. Li, X. Chen, W. Liu, Y. Wang, Z. Wu, C. Shan, J. Wu, Y. Zhang, P. Xi, D. Jin, Fast, live-cell imaging of 15 intracellular compartments by deep learning segmentation of super-resolution data, Biorxiv 1 (1) (Dec. 2021). doi:10.1101/2021.12.13.472520.
URL https://www.biorxiv.org/content/10.1101/2021.12.13.472520v1 15, 16, 17, 18, 19, 20, 28

[104] A. P. Dempster, The Dempster-Shafer calculus for statisticians, International Journal of Approximate Reasoning 48 (2) (2008) 365–377. doi:10.1016/j.ijar.2007.03.004. 15

[105] K. Van Den Dries, J. Fransen, A. Cambi, Fluorescence CLEM in biology: historic developments and current super-resolution applications, FEBS Letters 596 (19) (2022) 2486–2496. doi:10.1002/1873-3468.14421.
URL https://febs.onlinelibrary.wiley.com/doi/10.1002/1873-3468.14421 15

[106] G. Volpe, C. Wählby, L. Tian, M. Hecht, A. Yakimovich, K. Monakhova, L. Waller, I. Sbalzarini, C. Metzler, M. Xie, K. Zhang, I. Lenton, H. Rubinsztein-Dunlop, D. Brunner, B. Bai, A. Ozcan, D. Midtvedt, H. Wang, N. Sladoje, J. Bergman, Roadmap on Deep Learning for Microscopy, Arxiv, 2023. 15

[107] S. R. Cole, J. K. Edwards, S. Greenland, Surprise!, American Journal of Epidemiology 190 (2) (2021) 191–193. doi:10.1093/aje/kwaa136. 15

[108] L. Yang, Y. Huang, Z. Zhang, Y. Han, C. Kuang, Multicolor expansion fluorescence emission difference microscopy to reveal potential organelle contacts, Optics Communications 520 (2022) 128474. doi:10.1016/j.optcom.2022.128474.
URL https://www.sciencedirect.com/science/article/pii/S0030401822003261 16, 18, 28

[109] H. G. Damstra, B. Mohar, M. Eddison, A. Akhmanova, L. C. Kapitein, P. W. Tillberg, Visualizing cellular and tissue ultrastructure using Ten-fold Robust Expansion Microscopy (TREx), eLife 11 (2022) e73775. doi:10.7554/eLife.73775.
URL https://doi.org/10.7554/eLife.73775 16, 17, 18, 22, 27

[110] M. Damenti, G. Coceano, F. Pennacchietti, A. Bodén, I. Testa, STED and parallelized RESOLFT optical nanoscopy of the tubular endoplasmic reticulum and its mitochondrial contacts in neuronal cells, Neurobiology of Disease 155 (2021) 105361. doi:10.1016/j.nbd.2021.105361. 16, 18, 19, 28

[111] A. Shivanandan, A. Radenovic, I. F. Sbalzarini, MosaicIA: an ImageJ/Fiji plugin for spatial pattern and interaction analysis, BMC Bioinformatics 14 (1) (2013) 349. doi:10.1186/1471-2105-14-349.
URL https://doi.org/10.1186/1471-2105-14-349 16, 27

[112] A. Shivanandan, J. Unnikrishnan, A. Radenovic, Accounting for limited detection efficiency and localization precision in cluster analysis in single molecule localization microscopy, PLoS ONEISBN: 1932-6203 (Electronic)\r1932-6203 (Linking) (2015). doi:10.1371/journal.pone.0118767. 16

[113] A. M. Arnold, M. C. Schneider, C. Hüsson, R. Sablatnig, M. Brameshuber, F. Baumgart, G. J. Schütz, Verifying molecular clusters by 2-color localization microscopy and significance testing, Scientific Reports 10 (1) (2020) 4230. doi:10.1038/s41598-020-60976-6.
URL https://www.nature.com/articles/s41598-020-60976-6 16, 17, 18, 19, 20, 24

[114] J. Adler, S. N. Pagakis, I. Parmryd, Replicate-based noise corrected correlation for accurate measurements of colocalization, Journal of Microscopy 230 (1) (2008) 121–133. doi:10.1111/j.1365-2818.2008.01967.x.
URL https://onlinelibrary.wiley.com/doi/abs/10.1111/j.1365-2818.2008.01967.x 16

[115] M. D. Luecken, M. Büttner, K. Chaichoompu, A. Danese, M. Interlandi, M. F. Mueller, D. C. Strobl, L. Zappia, M. Dugas, M. Colomé-Tatché, F. J. Theis, Benchmarking atlas-level data integration in single-cell genomics, Nature Methods 19 (1) (2022) 41–50. doi:10.1038/s41592-021-01336-8.
URL https://www.nature.com/articles/s41592-021-01336-8 16

[116] J. P. Ioannidis, Why most published research findings are false, PLos

Medicine 2 (8) (2005) e124, publisher: Public Library of Science. 16

[117] A. Bompas, G. Powell, P. Sumner, Systematic biases in adult color perception persist despite lifelong information sufficient to calibrate them, Journal of Vision 13 (1) (2013) 19. doi:10.1167/13.1.19.
URL https://doi.org/10.1167/13.1.19 16

[118] I.-S. Lee, W.-H. Tsai, Data hiding in grayscale images by dynamic programming based on a human visual model, Pattern Recognition 42 (7) (2009) 1604–1611. doi:10.1016/j.patcog.2009.01.014.
URL https://www.sciencedirect.com/science/article/pii/S0031320309000429 16

[119] A. E. Silva, C. Chubb, The 3-dimensional, 4-channel model of human visual sensitivity to grayscale scrambles, Vision Research 101 (2014) 94–107. doi:10.1016/j.visres.2014.06.001.
URL https://www.sciencedirect.com/science/article/pii/S0042698914001370 16

[120] J. Fischer, D. Whitney, Serial dependence in visual perception, Nature Neuroscience 17 (5) (2014) 738–743. doi:10.1038/nn.3689.
URL https://www.nature.com/articles/nn.3689 16

[121] M. Bertalmío, A. Gomez-Villa, A. Martín, J. Vazquez-Corral, D. Kane, J. Malo, Evidence for the intrinsically nonlinear nature of receptive fields in vision, Scientific Reports 10 (1) (2020) 16277. doi:10.1038/s41598-020-73113-0.
URL https://www.nature.com/articles/s41598-020-73113-0 16

[122] S. Kastner, L. G. Ungerleider, The neural basis of biased competition in human visual cortex, Neuropsychologia 39 (12) (2001) 1263–1276. doi:10.1016/S0028-3932(01)00116-6.
URL https://www.sciencedirect.com/science/article/pii/S0028393201001166 16

[123] T. Blanc, H. Verdier, L. Regnier, G. Planchon, C. Guérinot, M. El Beheiry, J.-B. Masson, B. Hajj, Towards Human in the Loop Analysis of Complex Point Clouds: Advanced Visualizations, Quantifications, and Communication Features in Virtual Reality, Frontiers in Bioinformatics 1 (2022).
URL https://www.frontiersin.org/articles/10.3389/fbinf.2021.775379 16

[124] A. Spark, A. Kitching, D. Esteban-Ferrer, A. Handa, A. R. Carr, L.-M. Needham, A. Ponjavic, A. M. Santos, J. McColl, C. Leterrier, S. J. Davis, R. Henriques, S. F. Lee, vLUME: 3D virtual reality for single-molecule localization microscopy, Nature Methods 17 (11) (2020) 1097–1099. doi:10.1038/s41592-020-0962-1.
URL https://www.nature.com/articles/s41592-020-0962-1 16

[125] T. Rahbek-Clemmensen, M. D. Lycas, S. Erlendsson, J. Eriksen, M. Apuschkin, F. Vilhardt, T. N. Jørgensen, F. H. Hansen, U. Gether, Super-resolution microscopy reveals functional organization of dopamine transporters into cholesterol and neuronal activity-dependent nanodomains, Nature Communications 8 (1) (2017) 740. doi:10.1038/s41467-017-00790-3.
URL https://www.nature.com/articles/s41467-017-00790-3 16

[126] A. Mancebo, D. Mehra, C. Banerjee, D.-H. Kim, E. M. Puchner, Efficient Cross-Correlation Filtering of One- and Two-Color Single Molecule Localization Microscopy Data, Frontiers in Bioinformatics 1 (2021).
URL https://www.frontiersin.org/articles/10.3389/fbinf.2021.739769 17, 18, 19, 27

[127] Q. Chen, X. Shao, M. Hao, H. Fang, R. Guan, Z. Tian, M. Li, C. Wang, L. Ji, H. Chao, J.-L. Guan, J. Diao, Quantitative analysis of interactive behavior of mitochondria and lysosomes using structured illumination microscopy, Biomaterials 250 (2020) 120059. doi:10.1016/j.biomaterials.2020.120059.
URL https://www.sciencedirect.com/science/article/pii/S0142961220303057 18, 19, 22

[128] K. Bermudez-Hernandez, S. Keegan, D. R. Whelan, D. A. Reid, J. Zagelbaum, Y. Yin, S. Ma, E. Rothenberg, D. Fenyö, A Method for Quantifying Molecular Interactions Using Stochastic Modelling and Super-Resolution Microscopy., Scientific reports 7 (1) (2017) 14882, publisher: Nature Publishing Group. doi:10.1038/s41598-017-14922-8.
URL http://www.ncbi.nlm.nih.gov/pubmed/29093506 18, 19, 20, 25

[129] T. C. Kunz, R. Götz, S. Gao, M. Sauer, V. Kozjak-Pavlovic, Using Expansion Microscopy to Visualize and Characterize the Morphology of Mitochondrial Cristae, Frontiers in Cell and Developmental Biology 8 (2020).
URL https://www.frontiersin.org/articles/10.3389/fcell.2020.00617 18, 26, 27

[130] E. Arnold, S. Mozaffari, M. Dianati, Fast and Robust Registration of Partially Overlapping Point Clouds, IEEE Robotics and Automation Letters 7 (2) (2022) 1502–1509. doi:10.1109/LRA.2021.3137888. 19

[131] J. Gudmundsson, G. Narasimhan, M. Smid, Geometric Spanners, in: M.-Y. Kao (Ed.), Encyclopedia of Algorithms, Springer US, Boston, MA, 2008, pp. 360–364. doi:10.1007/978-0-387-30162-4_167.
URL https://doi.org/10.1007/978-0-387-30162-4_167 19, 22, 24

[132] B. L. Cheeseman, U. Günther, K. Gonciarz, M. Susik, I. F. Sbalzarini, Adaptive particle representation of fluorescence microscopy images, Nature Communications 9 (1) (2018) 5160. doi:10.1038/s41467-018-07390-9.
URL https://www.nature.com/articles/s41467-018-07390-9 19

[133] H. Shi, M. Drton, M. Hallin, F. Han, Semiparametrically Efficient Tests of Multivariate Independence Using Center-Outward Quadrant, Spearman, and Kendall Statistics, Arxiv 1 (1), arXiv:2111.15567 [math, stat] (Jan. 2023). doi:10.48550/arXiv.2111.15567.
URL http://arxiv.org/abs/2111.15567 20

[134] D. Bahr, D. Eschweiler, A. Bhattacharyya, D. Moreno-Andres, W. Antonin, J. Stegmaier, Cellcyclegan: Spatiotemporal Microscopy Image Synthesis Of Cell Populations Using Statistical Shape Models And Conditional Gans, in: 2021 IEEE 18th International Symposium on Biomedical Imaging (ISBI), IEEE, Nice, France, 2021, pp. 15–19. doi:10.1109/ISBI48211.2021.9433896.
URL https://ieeexplore.ieee.org/document/9433896/ 20

[135] R. Krueger, J. Beyer, W.-D. Jang, N. W. Kim, A. Sokolov, P. K. Sorger, H. Pfister, Facetto: Combining Unsupervised and Supervised Learning for Hierarchical Phenotype Analysis in Multi-Channel Image Data, IEEE transactions on visualization and computer graphics 26 (1) (2020) 227–237. doi:10.1109/TVCG.2019.2934547. 20

[136] M. Ankerst, M. M. Breunig, H.-P. Kriegel, J. Sander, OPTICS: ordering points to identify the clustering structure, ACM SIGMOD Record 28 (2) (1999) 49–60. doi:10.1145/304181.304187.
URL https://dl.acm.org/doi/10.1145/304181.304187 21, 23

[137] R. J. G. B. Campello, D. Moulavi, A. Zimek, J. Sander, Hierarchical Density Estimates for Data Clustering, Visualization, and Outlier Detection, ACM Transactions on Knowledge Discovery from Data 10 (1) (2015) 5:1–5:51. doi:10.1145/2733381.
URL https://doi.org/10.1145/2733381 21, 23

[138] E. Schubert, J. Sander, M. Ester, H. P. Kriegel, X. Xu, DBSCAN Revisited, Revisited: Why and How You Should (Still) Use DBSCAN, ACM Transactions on Database Systems 42 (3) (2017) 19:1–19:21. doi:10.1145/3068335.
URL https://doi.org/10.1145/3068335 21, 23

[139] B. Cardoen, H. Ben Yedder, S. Lee, I. R. Nabi, G. Hamarneh, DataCurator.jl: efficient, portable and reproducible validation, curation and transformation of large heterogeneous datasets using human-readable recipes compiled into machine-verifiable templates, Bioinformatics Advances 3 (1) (2023) vbad068. doi:10.1093/bioadv/vbad068.
URL https://academic.oup.com/bioinformaticsadvances/article/doi/10.1093/bioadv/vbad068/7188122 21

[140] J.-F. Gilles, T. Boudier, TAPAS: Towards Automated Processing and Analysis of multi-dimensional bioimage data, F1000Research 9 (2020) 1278. doi:10.12688/f1000research.26977.2. 21

[141] C. Allan, J.-M. Burel, J. Moore, C. Blackburn, M. Linkert, S. Loynton, D. Macdonald, W. J. Moore, C. Neves, A. Patterson, M. Porter, A. Tarkowska, B. Loranger, J. Avondo, I. Lagerstedt, L. Lianas, S. Leo, K. Hands, R. T. Hay, A. Patwardhan, C. Best, G. J. Kleywegt, G. Zanetti, J. R. Swedlow, OMERO: flexible, model-driven data management for experimental biology, Nature Methods 9 (3) (2012) 245–253. doi:10.1038/nmeth.1896. 21

[142] R. F. Laine, K. L. Tosheva, N. Gustafsson, R. D. M. Gray, P. Almada, D. Albrecht, G. T. Risa, F. Hurtig, A.-C. Lindås, B. Baum,

J. Mercer, C. Leterrier, P. M. Pereira, S. Culley, R. Henriques, NanoJ: a high-performance open-source super-resolution microscopy toolbox, Journal of Physics D: Applied Physics 52 (16) (2019) 163001. doi:10.1088/1361-6463/ab0261.
URL https://iopscience.iop.org/article/10.1088/1361-6463/ab0261 21

[143] D. J. Schodt, M. J. Wester, M. Fazel, S. Khan, H. Mazloom-Farsibaf, S. Pallikkuth, M. B. M. Meddens, F. Farzam, E. A. Burns, W. K. Kanagy, D. A. Rinaldi, E. Jhamba, S. Liu, P. K. Relich, M. J. Olah, S. L. Steinberg, K. A. Lidke, SMITE: Single Molecule Imaging Toolbox Extraordinaire (MATLAB), Journal of Open Source Software 8 (90) (2023) 5563. doi:10.21105/joss.05563.
URL https://joss.theoj.org/papers/10.21105/joss.05563 21

[144] A. Hofmann, M. Krufczik, D. Heermann, M. Hausmann, Using Persistent Homology as a New Approach for Super-Resolution Localization Microscopy Data Analysis and Classification of H2AX Foci/Clusters, International Journal of Molecular Sciences 19 (8) (2018) 2263. doi:10.3390/ijms19082263.
URL http://www.mdpi.com/1422-0067/19/8/2263 21

[145] H. Kobayashi, K. C. Cheveralls, M. D. Leonetti, L. A. Royer, Self-supervised deep learning encodes high-resolution features of protein subcellular localization, Nature Methods 19 (8) (2022) 995–1003. doi:10.1038/s41592-022-01541-z.
URL https://www.nature.com/articles/s41592-022-01541-z 21

[146] B. Midtvedt, J. Pineda, F. Skärberg, E. Olsén, H. Bachimanchi, E. Wesén, E. Esbjörner, E. Selander, F. Höök, D. Midtvedt, G. Volpe, Single-shot self-supervised object detection in microscopy, Nature Communications 13 (Dec. 2022). doi:10.1038/s41467-022-35004-y. 21

[147] G. M. I. Redpath, J. Rae, Y. Yao, J. Ruan, M. L. Cagigas, R. Whan, E. C. Hardeman, P. W. Gunning, V. Ananthanarayanan, R. G. Parton, N. Ariotti, Precision Super-Resolution Cryo-Correlative Light and Electron Microscopy for Rapid *in situ* Structural Analyses of Optogenetically-Positioned Organelles, Arxiv 1 (1) (Dec. 2022). doi:10.2139/ssrn.4309027.
URL https://papers.ssrn.com/abstract=4309027 21

[148] R. K. Vasudevan, M. Ziatdinov, L. Vlcek, S. V. Kalinin, Off-the-shelf deep learning is not enough, and requires parsimony, Bayesianity, and causality, npj Computational Materials 7 (1) (2021) 1–6. doi:10.1038/s41524-020-00487-0.
URL https://www.nature.com/articles/s41524-020-00487-0 21

[149] Y. Escoufier, Le Traitement des Variables Vectorielles, Biometrics 29 (4) (1973) 751–760. doi:10.2307/2529140.
URL https://www.jstor.org/stable/2529140 26

[150] F. Chen, P. W. Tillberg, E. S. Boyden, Expansion microscopy, Science 347 (6221) (2015) 543–548. doi:10.1126/science.1260088.
URL https://www.science.org/doi/10.1126/science.1260088 26, 27